General Disclaimer

One or more of the Following Statements may affect this Document

- This document has been reproduced from the best copy furnished by the organizational source. It is being released in the interest of making available as much information as possible.

- This document may contain data, which exceeds the sheet parameters. It was furnished in this condition by the organizational source and is the best copy available.

- This document may contain tone-on-tone or color graphs, charts and/or pictures, which have been reproduced in black and white.

- This document is paginated as submitted by the original source.

- Portions of this document are not fully legible due to the historical nature of some of the material. However, it is the best reproduction available from the original submission.

NASA CR-145193

STUDY OF DYNAMICS OF MINOR
CONSTITUENTS IN THE THERMOSPHERE

by

Joe M. Straus
Stephen P. Creekmore
Barbara K. Ching

MAY 1977

NASA

National Aeronautics and
Space Administration

THE AEROSPACE CORPORATION

STUDY OF DYNAMICS OF MINOR CONSTITUENTS IN THE THERMOSPHERE

By

Joe M. Straus
Stephen P. Creekmore
Barbara K. Ching

MAY 1977

By

Space Sciences Laboratory
THE AEROSPACE CORPORATION
El Segundo, CA 90245

for

NASA

National Aeronautics and
Space Administration

ABSTRACT

This report describes a numerical study of the global distribution of helium and argon in the terrestrial thermosphere. It is based on the extension of a three-dimensional single-fluid numerical model of the thermosphere previously developed by the authors to treat the dynamics of a minor gas imbedded in a background gas made up of N_2, O_2 and O. Empirical models of the upper atmosphere, based on satellite drag and mass spectrometer data, are used to specify the background gas density and temperature as functions of altitude, latitude and local time for a given day of the year. Effects of solar activity, eddy diffusion and exospheric transport on the global distribution of minor gases are investigated.

INTRODUCTION

In addition to the gases N_2, O_2, and O, which account for the great majority of the thermospheric composition in the altitude range between 90 and 500 km, there exist a multitude of trace gases of varying importance. Of these, considerable attention has been given to the chemically inert gases helium and argon. The interest in them arises primarily from the fact that they may be considered to be trace gases which have little influence on the dynamics of the upper atmosphere as a whole, but whose global distributions are very sensitive to global variations of wind, density and temperature fields as well as to eddy diffusion processes in the mesosphere and lower thermosphere. The present report describes three-dimensional numerical computations dealing with the global distributions of these minor constituents in the thermosphere.

A winter-summer asymmetry in the thermospheric helium concentration was first reported by Keating and Prior (1967, 1968). The earlier observations reported by Reber and Nicolet (1965) were shown there to be consistent with such a "winter helium bulge," and further aspects of the phenomenon were described by Keating, Mullins and Prior (1970, 1971) on the basis of analysis of the effects of atmospheric drag on the orbits of the satellites Explorers 9, 19, 24 and 39. Further measurements of the global distribution of thermospheric helium have been reported by Jacchia and Slowey (1968) from satellite drag data, by Shefov (1968) and

Tinsley (1968) using twlight observations of the helium 10830 Å emission, and by Reber et al. (1971), von Zahn et al. (1973), Hedin et al. (1974), Newton et al. (1975), Keating et al. (1975) and Mauersberger et al. (1976) using mass spectrometer data from satellites. Finally, relevant data from rocket-borne mass spectrometers have been reviewed by Kockarts (1973). Although the various measurements were made at different altitudes, local times, times of the year and phases of the solar cycle, the general feature of a winter helium enhancement is evident in all of them.

Considerably less observational data exist for argon than for helium. This is primarily because, with an atomic weight of 40 AMU, argon has such a short scale height in the thermosphere above the turbopause that its concentration is too small to measure at satellite altitudes above $\sim$300 km. Several rocket-borne mass spectrometers have detected argon (Schaefer, 1969; von Zahn and Gross, 1969; Hickman and Nier, 1972), but no global coverage was available prior to the launch of the ESRO-IV satellite in late 1972. Measurements reported by von Zahn et al. (1973) and von Zahn (1975) indicate that argon at 270 km altitude is more abundant in the summer hemisphere than the winter, with a summer/winter ratio of $\sim$10 there. They have pointed out that, although more measurements are required before a clear picture of the situation will exist, this behavior may be mainly due to argon's extreme sensitivity to global variations in temperature (i.e., scale height); thus, argon's

distribution may be dependent on wind fields in the thermosphere less than on global-scale temperature variations. Further mass-spectrometric measurements of thermospheric argon near the earth's equatorial plane were reported by Newton et al. (1975) on the basis of data taken by the San Marco 3 satellite. Although no information concerning global variations of argon could be obtained by this low-inclination satellite, argon was found to reach a maximum concentration at the equator in the middle afternoon ($\sim$15-16LT) and to vary diurnally by a factor of $\sim$3 at 280 km altitude. Furthermore, since the Ar maximum occurred approximately coincidentally with that of N_2, one may infer that the determination of the Ar distribution is dominated by the temperature distribution.

Reber and Nicolet (1965) suggested a seasonal variation in the turbopause altitude as the explanation for the winter-summer asymmetry in thermospheric helium. They noted that Kockarts and Nicolet (1972) has shown that an increase of 5 km in the turbopause altitude causes a factor of 2 decrease in the helium concentration above 200 km for a fixed atmospheric temperature. Kockarts (1972) pointed out that, if the helium concentrations determined from the OGO-6 mass spectrometer data (Hedin et al., 1974) were to be explained in this way, a factor of 50 variation in the eddy diffusion coefficient is needed. (This corresponds to a change in the turbopause altitude of approximately 25 km). An alternative explanation was proposed by Johnson and Gottleib (1970) on the basis of studies of the thermospheric energy budget. The observed warmth of the winter polar

region was shown to require downward atmospheric motion there; such a flow can be produced by upward motion in the summer hemisphere, horizontal flow across the equator and downward flow in the winter polar region. Associated with this circulation system would be a build-up of helium at high winter latitudes. The horizontal portion of this circulation pattern is similar to that determined by Geisler (1967) and subsequent investigators, and the recent three-dimensional model studies of Straus et al. (1975a) and Dickinson et al. (1975) indicate that the overall pattern of solstitial thermospheric motions described by Johnson and Gottleib (1970) can be generated by EUV heating.

Reber and Hays (1973) studied the effects of global-scale wind fields on the distribution of helium and argon. They treated the coupled momentum and continuity equations for a minor gas diffusing through a background gas whose vertical and horizontal velocities are parameterized in a simplified manner. Disregarding local-time variations, they showed that the latitudinal variations of helium concentration can be understood using the mechanism suggested by Johnson and Gottleib (1970). Furthermore, they demonstrated the effects of exospheric transport and solar activity on the helium distribution. The wind fields considered by Reber and Hays (1973) were chosen on the basis of their simplicity and possible resemblance to those which actually occur in the thermosphere. A more realistic approach to the problem was taken by Mayr and Volland (1973). They used a quasi-three dimensional perturbation model of a two-component thermosphere to study the diurnal variations of helium and atomic oxygen.

They showed that diffusion effects associated with global-scale wind fields increase the amplitudes of the diurnal variations of these species, and advance the local times of their diurnal maxima with respect to the major gas. Because the calculations applied to a single latitude, no latitudinal or seasonal variations could be treated.

The purpose of this report is to describe numerical investigations dealing with the dynamics of minor constituents in the thermosphere using a three-dimensional model which is considerably more realistic than those employed by previous investigators. The numerical model is an extension of a single-fluid model previously described by Creekmore et al. (1975) and Straus et al. (1975a) to treat the dynamics of a minor trace gas (such as He or A) in a background gas made up of N_2, O_2 and O in the altitude range 90-500km. The background gas density, mean molecular weight, and temperature are specified by empirical models based on satellite drag (CIRA, 1972) and/or mass spectrometer data from satellites (vz. ESRO-IV and OGO-VI). In the case of the models based on satellite-borne mass spectrometer data, a method of extending the existing empirical models downward to the 90 km level is described in the Appendix. The effects of exospheric transport, eddy diffusion and solar activity on the global variations of minor gas concentrations are discussed; comparisons of the numerical results with observational data are made.

Mathematical Model

The basis of the mathematical model employed here lies in the fact that the chemically inert minor constituents, He and Ar, have negligible effects on the dynamics and thermodynamics of the major constituents N_2, O_2 and O. For this reason, the density, temperature and wind fields of the major constituents may be determined once and for all, and the minor gas distributions may be calculated separately in a manner which includes the effects of major gases. In the computations to be described here, the temperature and density fields of the major gases have been taken from the empirical model of CIRA (1972) in the altitude range 90 to 500 km. Future studies will make use of the OGO-VI model of Hedin et al. (1974) and the ESRO-IV model (Keating et al., 1975) extended down to 90 km using the method described in the Appendix. In addition to simplifying the problem by allowing us to disregard thermodynamics, the use of an empirically-determined gas distribution is considered somewhat more realistic than that obtainable at present from a solution of the coupled equations of mass, momentum and energy conservation; as discussed at some length by Straus et al. (1975 a, b) and Dickinson et al. (1975), the various energy inputs into the thermosphere are not known to a degree necessary for quantitatively accurate global modeling of thermospheric density and temperature. The background gas is treated as a single gas whose density is the total of the N_2, O_2 and O densities and whose molecular weight is the mean

molecular weight given by the empirical model.

The background gas vertical and horizontal velocities are determined from solutions of the equations of mass and horizontal momentum conservation in a coordinate system rotating with the earth. Under steady-state conditions as viewed from the sun, the coordinates are r, the distance from the center of the earth, θ, the colatitude, and ϕ, the local time, and the equations are:

$$\Omega(\partial\rho/\partial\phi) + \nabla \cdot (\rho \underset{\sim}{v}) = 0 \tag{1}$$

$$\Omega(\partial\underset{\sim}{v}/\partial\phi) + \underset{\sim}{v} \cdot \nabla\underset{\sim}{v} + 2 \underset{\sim}{\Omega} \times \underset{\sim}{v} \tag{2}$$

$$= \underset{\sim}{g} - (1/\rho) \underset{\sim}{\nabla}p + (\mu/\rho) \nabla^2 \underset{\sim}{v} - \nu_{ni} (\underset{\sim}{v} - \underset{\sim}{v}_i)$$

where $\underset{\sim}{\Omega}$ is the angular velocity of the earth, ρ is the total background gas mass density, $\underset{\sim}{v}$ is the background gas velocity, $\underset{\sim}{g}$ is the acceleration due to gravity, p is the background gas pressure, μ is its viscosity, ν_{ni} is the neutral-ion collision frequency, and $\underset{\sim}{v}_i$ is the ion velocity. The viscosity μ is taken to be $\mu = 4.5 \times 10^{-4} (T/10^3)^{0.71}$ gm/cm-sec (Dalgarno and Smith, 1962), where T is the neutral temperature. Following Chapman (1956), we take $\nu_{ni} = 2.6 \times 10^{-9} M^{-1/2} n_i$, where M is the background gas mean molecular weight (AMU); the ion number density n_i is taken from the empirical ionospheric model of Ching and Chiu (1973). Assuming the absence of electric fields, the ion velocity is taken to be $\underset{\sim}{v}_i = (\underset{\sim}{v} \cdot \hat{b}) \hat{b}$ where $\hat{b}$ is the unit vector in the direction of the earth's magnetic field

(assumed to be a centered dipole aligned with the earth's rotation axis). The momentum conservation equation (2) is solved in the altitude range 90-500 km using the spectral method described by Creekmore et al. (1975). In short, it involves the expansion of each dependent variable in a series of orthonormal functions which are periodic in θ and ϕ and satisfy prescribed boundary conditions for that variable at 90 and 500 km. The (θ, ϕ) variations are described by scalar and vector spherical harmonics of order $n = 0, 1, 2$ and the radial variations are described by polynomials. After substitution of these expansions into the appropriate differential equations and projecting with each of the appropriate expansion functions, the solution of the steady-state problem involves the solution of a coupled set of nonlinear algebraic equations. This is accomplished through the use of the method of Marquardt (1963). In the case of equation (2), only the horizontal velocity components of $\underset{\sim}{v}$ are to be determined, since all of the other parameters are specified and the vertical velocity (which is to be calculated from equation (1)) has little effect on the horizontal velocity field $\underset{\sim\perp}{v}$. At the lower boundary, we assume that $\underset{\sim\perp}{v}$ vanishes with respect to the rotating earth, and at the upper boundary, we assume that the effects of viscosity are so important the radial derivative of $\underset{\sim\perp}{v}$ vanishes.

Once $\underset{\sim\perp}{v}$ is determined, the vertical velocity w can be calculated by integrating equation (1) in the form

$$(1/r^2) \, \partial(r^2 \rho w)/\partial r = -(1/r \sin \theta) \, \partial(\rho v_\theta \sin \theta)/\partial \theta \tag{3}$$

$$-(1/r \sin \theta) \, \partial(\rho v_\phi)/\partial \phi - \Omega \partial \rho/\partial \phi$$

8

downward from the 500 km level. In order to take into account the
effects of exospheric flow, the following boundary condition is imposed
on the vertical flux at 500 km (Hodges and Johnson, 1968):

$$(nw)\big|_{500} = (1 + 4/\epsilon_o)(k\Omega/g)\,\partial(nT/m)/\partial\phi \tag{4}$$

$$- (1 + 8.4/\epsilon_o)(k^2/g^2)\,\nabla_\perp^2\,(n\langle v\rangle\,T^2/m^2).$$

Here $n = \rho/m$, where m is the background gas mean molecular weight,
ϵ_o is the ratio of the radial distance to the 500 km level to the average
atmospheric scale height (kT/mg) there, k is Boltzmann's constant,
$\nabla_\perp^2$ is the horizontal Laplacian operator, and $\langle v\rangle = (2kT/m)^{1/2}$. Thus,
the vertical velocity determined in this way includes the effects of the
divergence of the horizontal wind field, the so-called "breathing" motion
of the atmosphere due to diurnal variations in the density, and lateral
transport in the exosphere.

Once the characteristics of the background gas are determined, the
global distribution of the minor constituents may be calculated in the
following manner. We assume that the minor gas temperature is equal
to that of the background gas. Furthermore, we assume that collisions
between the thermospheric constituents dominate the horizontal momentum
balance of the minor constituents to such an extent that the minor con-
stituents have the same horizontal velocity as the background gas; Mayr

and Volland (1973) have shown that this assumption is appropriate.
Thus, the determination of the minor gas distribution reduces to the
simultaneous solution of the coupled equations of mass and vertical
momentum conservation:

$$\Omega(\partial \rho_j / \partial \phi) + \nabla \cdot (\rho_j \underset{\sim}{v}_j) = 0 \tag{5}$$

$$\partial(\ln \rho_j)/\partial r + (Dm_j + Km)g/((D+K)kT) \tag{6}$$

$$+ (w_j - w)/(D+K) + (1 + \alpha_j) \; \partial(\ln T)\partial r = 0$$

Here, the subscripted variables refer to the minor gas, and the un-
subscripted variables refer to the background gas. The eddy diffusivity
is denoted K, the coefficient of thermal diffusion is α_j (α_j = -0.38 for
He and zero for other minor constituents), and we take $\underset{\sim}{v}_{\perp j} = \underset{\sim}{v}_\perp$, as noted
above. Finally, the molecular diffusion coefficient is taken to be (Kockarts,
1972):

$$D = 1.5 \times 10^{18}(\frac{1}{M_j} + \frac{1}{M})^{1/2} T^{1/2}/n \; (cm^2/sec)$$

where M_j and M are the minor constituent mass and the background gas
mean molecular weight in atomic mass units. The features of equation
(6) have been discussed in considerable detail by Kockarts (1972). In the
upper thermosphere, where D ≫ K, $\partial r = 0$ and D is very large, it reduces
to the familiar equation for hydrostatic equilibrium $(\partial \ln \rho_j/dr) = -m_j g/kT$.
However, in the lower thermosphere, these conditions do not hold, and

the effects of vertical diffusion (represented by the term involving $w_j - w$) and eddy mixing (represented by the eddy diffusion coefficient K) tend to cause departures from hydrostatic equilibrium.

These equations are solved simultaneously in the altitude range 90 to 500 km using the spectral method. The minor gas density at 90 km is taken to be fixed and equal to that given by the CIRA (1972) model: $\ln \rho_{He} = -33.45$ (i.e. $n_{He} = 4.42 \times 10^8/cm^3$) and $\ln \rho_A = -23.82$ (i.e. $n_A = 6.72 \times 10^{11}/cm^3$). At 500 km altitude, the vertical flux of the minor gas is specified by the requirement that flow in the exosphere conserves mass (i.e., there is no escape flux to infinity). Thus, the equivalent of equation (4) is used to specify the vertical velocity of the minor constituent at 500 km. This condition may be written

$$(\rho_j w_j)\big|_{500} = f_j(\theta, \phi) \tag{7}$$

since only properties of the atmosphere at 500 km are involved in the flux condition. This condition is satisfied by writing

$$w_j = \widehat{w}_j + f_j(\theta, \phi)/\rho_j$$

where $\widehat{w}_j$ is expanded as a product of spherical harmonics and vertical polynomials which vanish at 500 km.

THE MOTION OF THE BACKGROUND GAS

The motion of the background gas, when its density and temperature are fixed equal to that given by the empirical model CIRA (1972) has been studied by a number of investigators. (For recent discussion, see Blum and Harris, 1975 a, b, and Creekmore et al., 1975.) Above an isopycnic level near 113 km, the motion is generally directed from the pressure maximum at about 1430 hr. local time at the subsolar latitude towards the pressure minimum diametrically opposite. It flows over the poles and around the earth with a speed which generally increases with altitude to values on the order of 100-200 m/sec in the upper thermosphere. In the lower thermosphere (below the isopycnic level), the pressure gradients in the CIRA model are reversed, and the flow is directed in the opposite sense. The diurnal variation of the ion density leads to larger wind speeds at night than during the day, and the Coriolis force affects the flow at middle and high latitudes, especially at night, where ion drag effects are relatively unimportant. Figures 1 and 2 show the horizontal wind fields at several altitudes for values of the solar 10.7 cm flux $F_{10.7}$ of 140 and 70 x 10^{-22} w/m^2 - Hz (Zurich Sunspot number of $\sim$90 and $\sim$0, respectively). The general features of the flows in the two cases are quite similar, as is to be expected; the wind speeds are somewhat different, primarily because of differences in the ion density distributions and the size of the driving pressure gradients.

In order to satisfy the conservation of mass condition, vertical motions are induced in the thermosphere. As noted earlier, this vertical motion is produced by the divergence of the horizontal motion, by the diurnal rising and falling of isobaric surfaces and by the requirements of exospheric transport. The last of these effects dominates near the 500 km level, but the other two play increasingly important roles with decreasing altitude. Figures 3 and 4 illustrate the global variations of w at several altitudes for values of $F_{10.7}$ of 140 and 70×10^{-22} w/m^2 - Hz. In conjunction with the horizontal motion, the vertical motion is generally upwards at high latitudes in the summer hemisphere and downwards in the winter hemisphere. Flow velocities increase from a few cm/sec at 95 km altitude to several m/sec in the upper thermosphere. At all altitudes, the maximum upwards velocity occurs during the middle of the day (~9LT to 14LT), and the maximum downward velocity occurs during the middle of the night.

14

THE GLOBAL DISTRIBUTION OF HELIUM

If neither the background gas nor helium were to undergo vertical motion, the vertical helium density distribution at a given point in latitude and local time would be given by the hydrostatic relation:

$$d \ln \rho_{He}/dr = -(1 + \alpha_{He}) d \ln T/dr \tag{8}$$

$$-(D_{He} m_{He} + Km) g/\left((D_{He} + K) kT\right)$$

Under these conditions and assuming a constant value for the eddy diffusion coefficient K, the large value of the helium scale height $H_{He} = kT/m_{He} g$ leads to the fact that, at a given altitude, the helium density is fairly insensitive to global temperature variations. For example, at 500 km altitude, the CIRA (1972) model indicates a variation in the helium density of a factor of 1.29 for a variation of the exospheric temperature from $1000^{\circ}K$ to $1400^{\circ}K$. Furthermore, the density maximum occurs at the subsolar point. The failure of equation (8) in predicting both the magnitude and location of the winter helium bulge suggests the importance of vertical diffusion.

In order to determine the effects of vertical diffusion on the global helium distribution, the coupled equations of mass and vertical momentum conservation for helium, equations 5 and 6, must be solved simultaneously, the temperature, horizontal velocity and vertical velocity of the background

gas being specified. These equations have been solved over a representative range of values of the (globally constant) eddy diffusion coefficient K and 10.7 cm solar flux $F_{10.7}$ in the manner described previously.

Prior to presenting results of all of these calculations, Figure 5 demonstrates the considerable effects of vertical diffusion on the vertical distribution of helium in the thermosphere. This figure shows a comparison between the results of the solution of the hydrostatic equation (8) and that of the dynamic equations (5) and (6) for $F_{10.7}$ = 140 $w/m^2 Hz$, K = 10^7 cm^2/sec, K_p = 3. In contrast with the hydrostatic solution, in which there is little global helium variation at a fixed altitude, the dynamic solution indicates a global variation of about one order of magnitude at 500 km, with the maximum occurring in middle latitudes in the winter hemisphere and the minimum at the summer pole. In addition, it is important to note that the large global variation is produced at fairly low altitudes; the great majority of the departure from hydrostatic equilibrium occurs below ~200 km, and hydrostatic equilibrium prevails in the upper thermosphere. This is due to the rapid increase in molecular diffusivity D with altitude, which diminishes the effect of vertical diffusion in the upper thermosphere. The mechanism involved in this large effect has been discussed by Johnson and Gottleib (1970), Reber and Hays (1973) and Mayr and Volland (1973): the large-scale motion imposed on helium by the motion of the background gas

lead to its depletion in the summer hemisphere and build-up in the winter hemisphere.

The effects of exospheric transport, although not displayed here, are considerable. In order to evaluate its effect, a calculation which differed from that used to derive Figure 5 only in the treatment of the vertical flux at 500 km was carried out. In this calculation, the flux was taken to vanish everywhere on the 500 km spherical surface. The ratio of global maximum to minimum helium density at 500 km in this calculation was found to be 21, in excess by a factor of $\sim$2 with respect to that obtained when proper account of exospheric transport was taken.

Figures 6-9 show representative contour plots of the logarithm (base 10) of the calculated helium mass density at selected altitudes as a function of latitude and local time for several combinations of values of $F_{10.7}$ and K under June solstice conditions. At the lowest altitudes, the global He variation is dependent on the (constant) boundary conditions used, and so the significance of the results there should not be over-estimated. However, the results in the middle and upper thermosphere indicate that a notable winter helium bulge occurs for all choices of values of $F_{10.7}$ and K. The global maximum He density at a fixed altitude occurs at middle-to-high winter latitudes, and the minimum occurs at high summer latitudes. The local time of maximum He density at a given altitude is $\sim$6 - 10 LT, dependent on altitude, the maximum occurring somewhat later with increasing altitude. These

results are in excellent agreement with the observational data taken by the OGO-VI mass spectrometer (Hedin et al., 1974) and the ESRO IV gas analyzer (Keating et al., 1975).

The general effect of variations of K is evident from comparison of Figures 6 and 7, both of which represent calculations with $F_{10.7} = 140$ w/m^{2}Hz, but with values of K = 3 x 10^6 cm^2/sec (Fig. 6) and 6 x 10^6 cm^2/sec (Fig. 7); these values of K correspond to turbopause altitudes (where K = D) of ~106 km and ~110 km, respectively. At middle and high altitudes, the results of these calculations are very similar in their global distributions of He. To a large extent, the only difference lies in the shift of He density by a factor of ~2, the values corresponding to K = 3 x 10^6 cm^2/sec being higher. This is due to the effects of eddy diffusion in the lower thermosphere: the higher the value of K, the higher in altitude do the effects of turbulence tend to mix the atmosphere. Thus, for high values of K, the He density decreases with altitude with the scale height of the mixed gas (whose molecular weight is ~29), rather than with its own scale height (which is a factor of ~7 larger than that of the mixed gas). Thus, the He density in the thermosphere decreases (at a given altitude) with increasing K. Other than this shift, the global distribution of He in the two cases is quite similar; for example, at 490 km altitude, the ratio of global maximum to global minimum He density is ~7.2 for K = 3 x 10^6 cm^2/sec and ~8.4 for K = 6 x 10^6 cm^2/sec.

(It is 9.6 for $K = 10^7$ cm^2/sec.) These results indicate a relatively weak effect of variation in the (constant) value of K on the magnitude of the winter helium bulge.

The effect of variation in the value of $F_{10.7}$ is considerably larger than that due to variation in K. Figures 8 and 9 show results of calculations with $K = 10^7$ cm^2/sec, $F_{10.7} = 100$ and 70×10^{-22} w/m^2 Hz, respectively. Once again, little significance should be placed on the results at the 95 km altitude, but comparison of corresponding figures at higher altitudes shows that the ratio of global maximum to minimum helium densities increases strongly with decreasing $F_{10.7}$. For more detailed comparison, Table 1 gives the value of this ratio at selected altitudes for $K = 10^7$ cm^2/sec, $F_{10.7} = 140$, 100 and 70×10^{-22} w/m^2 Hz. The decrease of the ratio at all altitudes with increasing $F_{10.7}$ is clear. The decrease of the ratio with $F_{10.7}$ is due to the fact that exospheric transport (which tends to smooth out large global variations of the helium density distribution) increases strongly with exospheric temperature, and thus with $F_{10.7}$. Also notable is the fact that (for a given set of values of $F_{10.7}$ and K) the ratio reaches a maximum at ~250-300 km altitude and then decreases to a fairly constant value above 400 km.

Table 1: Ratios of helium densities ($K = 10^7 \text{ cm}^2/\text{sec}$)

altitude km	$F_{10.7} = 140$	$F_{10.7} = 100$	$F_{10.7} = 70$
120	1.8	2.8	4.5
150	6.7	10.9	19.1
205	14.0	23.4	41.6
265	14.6	25.0	46.1
320	11.0	20.3	37.5
380	9.4	17.4	33.3
430	9.7	17.9	35.0
470	9.7	18.0	35.6
490	9.7	17.8	35.3

Figure 10 gives a comparison of the results of our model calculations with mass-spectrometer data reported by several investigators. The values marked "model" are the calculated ratios at the altitudes at which the experimental results were reported. The agreement is reasonably good, the slope of the curve between the model values being somewhat larger than that indicated by the data. The comparability of the model and experimental results may not be exact, however, because the ratios plotted for the experimental data represent the ratio as observed, which may not be a truly global ratio because of orbital considerations.

Comparison with observational data may also be made with the data from the mass spectrometer carried by the low-inclination San Marco 3

satellite. Newton et al. (1975) report that the diurnal maximum He

density in the 220-280 km altitude range at the equator occurs at

~7.5 hrs. local time. This is in excellent agreement with the

results of our model calculations. Furthermore, they report that

the ratio of daily maximum to minimum He density at the equation is

~1.7-1.8. This is slightly in excess of the value of 1.55-1.65

(dependent on $F_{10.7}$ and K) derived from the present numerical

calculations.

Finally, Keating et al. (1973) have reported a north-south asymmetry

in the global helium distribution. On the basis of atmospheric drag data

from the Explorers 9, 19, 24 and 39 satellites, they found that helium

concentrations in local summer at high latitudes are more than 50%

lower in the southern hemisphere than in the northern hemisphere;

furthermore, the increase in helium concentrations from summer to

winter was found to be ~80% greater in the southern hemisphere than

in the winter hemisphere. If the global helium distribution is determined

primarily by global circulation, this effect should be caused by outflow

from the southern hemisphere in December that is larger than the

corresponding outflow from the northern hemisphere in June. In

order to evaluate this mechanism, we carried out computations at

December solstice, to be compared with those previously described

for June. Using the CIRA (1972) model to specify the background gas

density and temperature distributions, we found a negligible difference

in the global circulation pattern between June and December solstice

21

other than, of course, the fact that the flow is in opposite directions. Thus, no north-south asymmetry of He can be explained in the present calculations. This negative result is not surprising, since the CIRA (1972) model has no north-south asymmetry, and only a very slight asymmetry in the wind field can be generated (through the effect of ion drag) by the small asymmetries present in the ion density model used here. However, more accurate models of upper-atmospheric density, such as newer models based on mass-spectrometer data, do show some north-south asymmetry, which may be expected to drive an asymmetry in the winter helium bulge. Investigation of the effects of this asymmetry will be a subject of future work.

THE GLOBAL DISTRIBUTION OF ARGON

If neither the background gas nor argon were to undergo vertical motion, the vertical argon density distribution at a given point in latitude and local time would be given by the hydrostatic relation:

$$d\ln\rho_A/dr = d\ln T/dr - (D_A m_A + Km)g/\left((D_A + K)kT\right). \qquad (9)$$

Under these conditions, and assuming a constant value for the eddy diffusion coefficient K, the small value of the argon scale height causes the argon density at a given altitude to be extremely sensitive to global temperature variations. For example, at 250 km altitude, the CIRA (1972) model indicates a variation in the argon density by a factor of ~5.2 for a variation in exospheric temperature from 800°K to 1000°K, the maximum density occurring at the location of maximum exospheric temperature. At 400 km altitude, this variation has increased to a factor of ~45. Thus, as von Zahn (1975) has pointed out, the observed global variation of argon may be explained to a large extent on the basis of temperature (scale height) variations alone.

The extreme sensitivity of the argon distribution to temperature variations implies that, in order to treat the argon distribution quantitatively, including the effects of vertical diffusion, one must have an accurate model of thermospheric temperatures, especially in the lower thermosphere. Since such a model does not exist because of the

unavailability of data at altitudes below ~ 200 km, only a semi-quantitative study of argon can be carried out. Figure 11 indicates the magnitude of the effects of vertical diffusion on the vertical distribution of thermospheric argon. This figure shows a comparison between the results of the solution of the hydrostatic equation (9) and that of the dynamic equations (5) and (6) for $F_{10.7} = 100 \times 10^{-22}$ w/m^2 Hz, $K = 10^7$ cm^2/sec, $K_p = 3$. The dynamic solution indicates that vertical diffusion below ~ 200 km can cause departures from hydrostatic equilibrium in the vertical argon distribution, but that hydrostatic equilibrium prevails above that altitude. Thus, the vertical distribution of argon density could be used to infer thermospheric temperatures above ~ 250 km altitude, but departures from hydrostatic equilibrium preclude such an analysis below that altitude.

Figure 11 shows representative contour plots of the logarithm (base 10) of the calculated argon mass density at selected altitudes as a function of latitude and local time for $F_{10.7} = 100 \times 10^{-22}$ w/m^2 Hz, $K = 10^7$ cm^2/sec under June solstice conditions. As in the case of helium, little emphasis should be placed on the results at 95 km, but at higher altitudes, a definite pattern appears: the argon density is maximal at 14-16 LT at the summer pole and minimal at low southern (winter) latitudes at ~ 4 LT. The ratio of maximum to minimum global argon density increases from ~ 5.5 at 155 km to ~ 85 at 265 km (and increases further at higher altitudes). This variation is somewhat stronger than that explainable on the basis of hydrostatic equilibrium and indicates that global circulation may be able to reinforce the effect due to temperature variation. Furthermore, the fact that the maximum occurs at the summer pole, and not at the subsolar latitude,

24

where the temperature is maximum demonstrates the effects of global winds on the argon distribution.

Comparison with the data reported by Newton et al. (1975) from the San Marco 3 mass spectrometer can be made for equatorial latitudes. Our model calculations indicate that the local times of maximum and minimum argon density at a fixed altitude are well-predicted by the model, but that the calculated diurnal variation of about one order of magnitude at 280 km altitude is somewhat larger than that observed. Such a discrepancy is probably due to inaccurate determination of the vertical diffusion velocity of argon in the lower thermosphere due to the inadequacy of the CIRA model there.

In order to investigate the effects of exospheric transport on the argon distribution, a calculation identical to the one described above was carried out with the argon flux at the 500 km altitude arbitrarily set to zero. The difference between the results obtained and those described above was found to be negligible, indicating the unimportance of exospheric transport in determining the global argon distribution. This result was also found by Reber and Hays (1973) and is attributed to the large atomic mass of argon, which causes argon to have a relatively small exospheric flux. Furthermore, since its scale height is small, any effect of exospheric flow vanishes far above the region in which vertical diffusion can affect its vertical distribution (i.e. below ~200 km).

SUMMARY

In this report, we have described numerical calculations dealing with dynamical effects on the global distribution of the thermospheric minor constituents helium and argon. The CIRA (1972) empirical model of the upper atmosphere has been used to specify the temperature, density and mean molecular weight of a background gas made up of N_2, O_2 and O. The conservation of momentum equations are solved to determine the horizontal and vertical velocities of the background gas. The temperature and horizontal velocity of the minor constituents are assumed to be equal to those of the background gas, and the equations of conservation of mass and vertical momentum are solved to determine the minor gas vertical velocity and density. The effects of solar activity, eddy diffusion and exospheric transport on the global distributions of minor constituents are treated.

It has been shown that the qualitative features of the observed global distribution of helium can be understood as being primarily due to the effects of global-scale winds that blow from the summer hemisphere to the winter hemisphere. The computed helium distribution shows a strong winter helium bulge whose amplitude increases with decreasing solar activity (for fixed eddy diffusivity) and with increasing eddy diffusivity (for fixed solar activity). Major departures from diffusive equilibrium occur below about 200 km altitude, where the molecular diffusivity is still small enough that diffusion velocities are important.

Quantitative comparison of the results of the calculations with observational data indicates that there are some discrepancies, but that the major observed features are reproduced. Inadequacies in the lower thermosphere of the empirical model of the background gas probably cause the majority of the discrepancies.

In the case of argon, the situation is somewhat different. The argon distribution is less sensitive to thermospheric wind fields than it is to global temperature distributions which cause its scale height to vary. Thus, the computed argon distribution is extremely dependent on the empirical model of thermospheric temperature. In spite of this difficulty, the general features of the observed global argon distribution are reproduced by the numerical model.

All of the calculations described here made use of the CIRA (1972) model for specification of the global distribution of the background gas. Models based on satellite-borne mass spectrometer data will be used in the future to provide this input. (A method for extending these models down to the 90 km level is discussed in the Appendix of this report.) Because of the sensitivity of the distribution of minor constituents to the properties of the background gas, comparison of the results of calculations using the various empirical models will be of interest.

Finally, it is of note that no treatment of the effects of globally varying eddy diffusivity has been carried out in the work described here. As noted earlier, this possible variation can have considerable effect on

the distributions of minor constituents, and the effects of this variation probably act in addition to those of the transport mechanism treated here. The inclusion of a global model of eddy diffusivity, if it can be formulated using a data base other than that derived from observations of minor constituents, is straightforward.

Acknowledgements

The authors would like to thank Dr. D. R. Hickman for a number of useful discussions and Dr. R. M. Harris for aid in developing and running the computer program.

References

Alcayde, D., P. Bauer, and J. Fontanari, "Long-term Variations of Thermospheric Temperature and Composition," *J. Geophys. Res.*, 79, 629, 1974.

Bates, D. R., "Some Problems Concerning the Terrestrial Atmosphere above about 100 km Level," *Proc. Roy. Soc. London*, A253, 451, 1959.

Blum, P. W. and I. Harris, "Full Nonlinear Treatment of the Global Thermospheric Wind System," *J. Atmos. Terr. Phys.*, 37, 193 and 213, 1975.

Chapman, S., "The Electrical Conductivity of the Ionosphere," *Nuovo Cimento*, 4, 1385, 1956.

Ching, B. K. and Y. T. Chiu, "A Phenomenological Model of the Global Electron Density in the E, F1 and F2 Regions," *J. Atmos. Terr. Phys.*, 35, 1615, 1973.

CIRA, *COSPAR International Reference Atmosphere*, Akademie-Verlag, Berlin, 1972.

Creekmore, S. P., J. M. Straus, R. M. Harris, B. K. Ching and Y. T. Chiu, "A Global Model of Thermospheric Dynamics, I. Wind and Density Fields Derived from a Phenomenological Temperature," *J. Atmos. Terr. Phys.*, 37, 491, 1975.

Dalgarno, A. and F. J. Smith, "The Thermal Conductivity and Viscosity of Atomic Oxygen," *Planet. Space Sci.*, 9, 1, 1962.

Dickinson, R. E., E. C. Ridley and R. G. Roble, "Meridional Circulation in the Thermosphere, I. Equinox Conditions," *J. Atmos. Sci.*, 32, 1737, 1975.

Geisler, J. E., "A Numerical Study of the Wind System in the Middle Thermosphere," *J. Atmos. Terr. Phys.*, 29, 1469, 1967.

Gross, J. and U. von Zahn, "Air Density and Composition in the Lower Thermosphere Above Fort Churchill," *Space Res.* 11, 875, 1971.

Groves, G. V., "Atmospheric Structure and its Variations in the Region from 25 to 120 km," *CIRA*, Berlin: Akademie-Verlag, 1972.

Hedin, A. E., H. G. Mayr, C. A. Reber, N. W. Spencer and G. R. Carignan, "Empirical Model of Global Thermospheric Temperature and Composition Based on Data from the OGO-6 Quadrupole Mass Spectrometer," J. Geophys. Res., 79, 215, 1974.

Hickman, D. R. and A. O. Nier, "Measurement of the Neutral Composition of the Lower Thermosphere above Fort Churchill by Rocket-Borne Mass Spectrometer," J. Geophys. Res., 77, 2880, 1972.

Hodges, R. R. and F. S. Johnson, "Lateral Transport in Planetary Exospheres," J. Geophys. Res., 73, 7307, 1968.

Jacchia, L. G. and J. W. Slowey, "Diurnal and Seasonal Latitudinal Variations in the Upper Atmosphere," Planet. Space Sci., 16, 509, 1968.

Johnson, F. S., and B. Gottleib, "Eddy Mixing and Circulation at Ionospheric Levels," Planet. Space Sci., 18, 1707, 1970.

Keating, G. M. and E. J. Prior, "Latitudinal and Seasonal Variations in Atmospheric Densities Obtained During Low Solar Activity by Means of the Inflatable Air Density Satellites," Space Res., 7, 1119, 1967.

Keating, G. M. and E. Prior, "The Winter Helium Bulge," Space Res., 8, 982, 1968.

Keating, G. M., J. A. Mullins and E. J. Prior, "The Polar Exosphere During Solar Minimum," Space Res., 10, 439, 1970.

Keating, G. M., J. A. Mullins and E. J. Prior, "Simultaneous Measurements of Exospheric Densities near Opposite Poles," Space Res., 11, 987, 1971.

Keating, G. M., D. S. McDougal, E. J. Prior and J. S. Levine, "North-South Asymmetry of the Neutral Exosphere," Space Res., 13, 327, 1973.

Keating, G. M., E. J. Prior, J. Y. Nocholson, H. Trinks, "Thermospheric Model of Helium and Molecular Nitrogen Based on ESRO-IV Gas Analyzer Measurements," Trans. Am. Geophys. Union, 56, 407, 1975.

Kockarts, G., "Distribution of Hydrogen and Helium in the Upper Atmosphere," J. Atmos. Terr. Phys., 34, 1729, 1972.

Kockarts, G., "Helium in the Terrestrial Atmosphere," Space Sci. Rev., 14, 723, 1973.

Kockarts, G. and M. Nicolet, "Aeronomical Problem of Neutral Helium and Hydrogen," Ann. Geophys., 18, 269, 1962.

Marquardt, D. W., "An Algorithm for Least-Squares Estimation of Nonlinear Parameters," J. Soc. Ind. Appl. Math., 11, 431, 1963.

Mauersberger, K., D. C. Kayser, W. E. Potter and A. O. Nier, "Seasonal Variation of Neutral Thermospheric Constituents in the Northern Hemisphere," J. Geophys. Res., 81, 7, 1976.

Mayr, H. G. and H. Volland, "A Two-Component Model of the Diurnal Variations in the Thermospheric Composition," J. Atmos. Terr. Phys., 35, 669, 1973.

Newton, G. P., W. T. Kasprzak, S. A. Curtis and D. T. Pelz, "Local Time Variation of Equatorial Thermospheric Composition Determined by the San Marco 3 NACE," J. Geophys. Res., 80, 2289, 1975.

Reber, C. A. and Nicolet, "Investigation of the Major Constituents of the April-May 1963 Heterosphere by the Explorer 17 Satellite," Planet. Space Sci., 13, 617, 1965.

Reber, C. A., D. N. Harpold, R. Horowitz and A. E. Hedin, "Horizontal Distribution of Helium in the Earth's Upper Atmosphere," J. Geophys. Res., 76, 1845, 1971.

Reber, C. A. and P. B. Hays, "Thermospheric Wind Effects on the Distribution of Helium and Argon in the Earth's Upper Atmosphere," J. Geophys. Res., 78, 2977, 1973.

Rugge, H. R. and B. K. Ching, "Atmospheric Density from the Low Altitude Satellite 1970-48A: Comparison of Orbital Decay Measurements, Accelerometer Measurements, and Atmospheric Models," Planet. Space Sci., 23, 323, 1975.

Schaefer, E. J., "Composition and Temperature of the Neutral Tropical Lower Thermosphere," J. Geophys. Res., 74, 3488, 1969.

Shefov, N. N., "Twilight Helium Emission During Low and High Geomagnetic Activity," Planet. Space Sci., 16, 1103, 1968.

Straus, J. M., S. P. Creekmore, R. M. Harris, B. K. Ching and Y. T. Chiu, "A Global Model of Thermospheric Dynamics, II. Wind, Density, and Temperature Fields Generated by EUV Heating," J. Atmos. Terr. Phys., 37, 1245, 1975a.

Straus, J. M., S. P. Creekmore, R. M. Harris and B. K. Ching, "Effects of Heating at High Latitudes on Global Thermospheric Dynamics," J. Atmos. Terr. Phys., 37, 1545, 1975b.

Tinsley, B. A., "Measurements of Twilight Helium 10830 A Emission,"
Planet. Space Sci., 16, 91, 1968.

von Zahn, U., K. H. Fricke and H. Trinks, "ESRO-4 Gas Analyzer
Results 1. First Observation of the Summer Argon Bulge," J.
Geophys. Res., 78, 7560, 1973.

von Zahn, U., "Early Aeronomy Results from the Satellite ESRO 4,"
in Atmospheres of Earth and the Planets, ed. by B. M. McCormac,
Dordrecht: D. Reidel, 1975.

APPENDIX

Extrapolation of the OGO-VI Atmospheric Model

Jacchia-type Temperature Profiles

The OGO-VI empirical model of atmospheric temperature and
composition (Hedin et al., 1974) has been modified so as to extend
down to 90 km altitude and to include O_2. These revisions allow this
model to be used to specify background gas quantities required in the
study of minor constituents in the thermosphere. To provide a better
perspective of the discussion to follow, it is instructive to review
briefly the OGO-VI model and also the CIRA (1972) model, as the
method of extrapolation was patterned after the latter model.

The OGO-VI model is based on mass spectrometer observations
of the behavior of the atmospheric constituents N_2, O and He at altitudes
above ~ 400 km. The quantities specified by the model are the con-
centrations of the aforementioned species and the exospheric temperature
T_∞. The exospheric temperature is inferred from the behavior of the
N_2 density assuming certain boundary conditions on N_2 and T, and a
certain functional dependence of T on altitude z. The exospheric
temperature given by the model is thus only a "virtual" temperature,
but comparisons with incoherent scatter observations indicate that
the model temperature is consistent with the data, at least at the
location of Millstone Hill. Assuming a Bates (1959) temperature
profile, Hedin et al. (1974) extrapolated their high altitude data down

to 120 km, where they assumed that both N_2 and T were fixed. He
and O were not constrained to be constant at the lower boundary, but
were allowed to vary spatially and temporally in order to reproduce
the observed high altitude behavior.

The CIRA (1972) is based primarily on satellite drag measure-
ments of total density. The data base for this model covers a greater
range in altitude and real time than that of the OGO-6 model. However,
data from low-altitudes (< 250 km) and high latitudes are very sparce.
In contrast to the OGO-VI model, CIRA starts at 90 km, where all
atmospheric variables are held constant. Assuming certain boundary
values and the height dependence for the temperature, Jacchia empirically
deduced the exospheric temperature required to reproduce the observed
total density. As in the OGO-VI model, the CIRA temperature is also a
virtual quantity. The temperatures of the two models are similar on
average; however, there are significant seasonal-latitudinal differences.
We shall describe a method of extrapolating the high altitude OGO-VI
observations downwards to obtain a plausible (though not necessarily
"correct") low altitude model without imposing constant conditions at
120 km.

First, we obtain the OGO-VI model values of the concentrations
of N_2, He and O at 450 km and the exospheric temperature. These
quantities are functions of space and time, being dependent on latitude,
local time, day of the year, and indices of solar and geomagnetic
activity. The OGO-VI exospheric temperature field T_∞ is accepted

a priori (even though it is an inferred parameter, dependent on a number of assumptions) and is used to derive the vertical temperature distribution as formulated in CIRA (1972).

Once the temperature profile is established, the vertical distributions of N_2, He and O can be computed in the region of diffusive equilibrium, which is assumed to begin at 100 km altitude:

$$\ln \frac{n(i)}{n^*(i)} + (1 + \alpha_i) \ln \frac{T}{T^*} = - \int_{z^*}^{z} \frac{M_i g}{RT} \, dz \tag{A1}$$

where the asterisk ($*$) denotes quantities at 450 km as prescribed by the OGO-VI model, and $\alpha_i = -0.38$ for He and $\alpha_i = 0$ for N_2 and O.

Once $n(N_2)$ is obtained (from eq. A1), $n(O_2)$ is determined using

$$n(O_2) = n(N_2) \, R' \left[\frac{n(N_2) T}{n'(N_2) T'} \right]^{(\mu-1)} \tag{A2}$$

where primed quantities are evaluated at $z' = 150$ km, R' is the O_2/N_2 ratio at z' (assumed to be 0.1), and $\mu = m(O_2)/m(N_2) = 32/28$.

The number densities and hence the mean molecular mass M of the atmosphere are now established above a height of 100 km. The concentrations below 100 km depend on the value of M at 100 km. Since there is little reliable data on the lower thermospheric composition, we assume simply that M increases linearly from its 100 km value to a constant value of 28.83 at the lower boundary of 90 km. The total

pressure p in the mixing region is given by

$$\ln \left(\frac{p}{p_o} \right) = -\int_{z_o}^{z} \frac{Mg}{RT} \, dz \qquad (A3)$$

where $p_o = \rho_o R T_o / M_o$

Here, R is the universal gas constant, and ρ_o, T_o, and M_o are assumed constant and equal to values prescribed in the CIRA model, namely

$$T_o = 183 \, {}^{o}K$$

$$M_o = 28.83$$

$$\rho_o = 3.46 \times 10^{-9} \, gm/cm^3$$

The concentrations follow immediately:

$$n(N_2) = f_1 \beta N$$

$$n(O_2) = N \left[\beta (1 + f_2) - 1 \right]$$

$$n(O) = 2N (1 - \beta)$$

$$n(He) = f_3 \beta N$$

where $\qquad N = p/kT \qquad$ (k = Boltzmann constant)

$\beta = M/M_s \qquad$ (M_s = mean mass at sea level, = 28.96)

$$f_1 = 0.78110$$

$$f_2 = 0.20955$$

$$f_3 = 6.147 \times 10^{-6}$$

The constants f_i are sea level fractions (by volume) of the various species.

It is perhaps of greatest interest to examine details of the model at low thermospheric altitudes, where observational data are scarce and where much reliance must be placed on predictive models. To avoid confusion with the original OGO-VI model, we shall refer to the newly extrapolated model as JACOGO, in recognition of the fact that it combines features of both the CIRA model as formulated by Jacchia and the OGO-VI model.

In the middle and upper thermosphere (above about 250 or 300 km) the OGO-VI and JACOGO models are very similar, which is to be expected since the temperature at these altitudes is near its thermopause value (i.e. the exospheric temperature, which is identical for both models). In the lower thermosphere differences will arise because of the different lower boundary conditions and vertical temperature profiles. Figure 13 illustrates the differences between the Bates temperature profile (used in OGO-VI) and the Jacchia temperature profile used in JACOGO for two values of the exospheric temperature, 1000 and 1300 $^{\circ}$K. Under

average solar and geomagnetic conditions ($F_{10.7}$ = 150, Kp = 1) these temperatures would approximate the diurnal range at low latitudes during equinox. Under solstice conditions, the diurnal range is somewhat larger, about 800 to 1300 $^{\circ}$K.

The global distribution of atomic oxygen at 120 km from JACOGO is shown in Figs. 14a and 14b for the June solstice and September equinox, respectively. The distributions are very similar to those presented by Hedin et al. (1974) despite the use of different temperature profiles and boundary conditions. That is, the O density at equinox is largest near the equator, but during the solstice is largest at high winter latitudes. The ratios of the global maximum to minimum O density are roughly the same for the two models: ~2 during equinox and ~4 during solstice. The major difference between the models concerns the magnitude of the O density: the global average (i. e. latitude and local time average) from JACOGO is ~25% greater than that from OGO-VI during the September equinox. It is interesting to note that the global average predicted by JACOGO is approximately half-way between the values predicted by CIRA and OGO-VI.

The global distributions of N_2 at 120 km from JACOGO are shown in Figs. 15a and 15b for the September equinox and June solstice. The predicted N_2 density is found to vary globally by a factor of 1.6 to 2.0 during equinox and solstice, respectively. In the original OGO-VI model, N_2 is assumed to be constant at 120 km; in the CIRA model N_2 varies globally but by only about 10% or less. The N_2 distributions shown in

Figs. 15a and 15b have some unexpected properties. First, in the equinoctial case the local-time averaged density increases nearly monotonically with latitude in going from south to north. Intuitively, one would expect symmetry about the equator and maximum densities at the equator. (The O distribution in Fig. 14b also exhibits an asymmetry in that the north polar densities exceed those in the south by about 40%.) Now, since the exospheric temperature distribution is essentially symmetrical and constant boundary conditions are assumed at 90 km, these asymmetrical properties must originate from similar asymmetries in the 450-km concentrations of the OGO-VI model.

Another unusual property of the N_2 distribution, which may be seen in Fig. 15a, is that during solstice the major global maximum and minimum are located at mid-to-high winter latitudes. This behavior is not strictly like the O distribution, in which the maximum and minimum are in opposite hemispheres. Now, since low altitude observations indicate that winter densities are higher than summer densities (e.g. Groves, 1972), it is tempting to speculate that the N_2 distribution in Fig. 15a is consistent with such data. Calculated contours for other days of the year indicate, however, that the extrapolated 120-km behavior is not strictly seasonal (annual), but contains subannual harmonic components not seen in the data of Groves. The JACOGO variations at 120 km are also different from those of CIRA, even though the two models are identical at 90 km. It must be concluded, therefore, that the detailed behavior of the lower atmosphere, as predicted by the JACOGO model,

is induced artificially by the particular combination of features of the OGO-VI and CIRA models, and thus the results should not be construed as reflecting actual conditions.

It is important to note that, insofar as the present applications are concerned, the small scale features shown in Figs. 14 and 15 are not resolved by our numerical model but are smoothed out. The global average JACOGO density agrees with that of CIRA to within 7%. A number of comparisons of low altitude density measurements have indicated that the CIRA model density is correct to within 10% or 20% on average. On the other hand, the OGO-VI model at 143 km has been found to underestimate the density by a factor of 1.7 (Rugge and Ching, 1975).

ADDENDUM

The calculations described in the main body of this report make use of the CIRA (1972) model for specifying the background gas temperature and density distributions. The calculations were carried out in the altitude range 90-500 km and were applicable for values of the solar 10.7 cm flux in the range 70 to 140 x 10^{-22} w/m^2 Hz. The results of these computations were compared with helium distributions as measured by the satellites OGO-6, ESRO-4 and AE-C. Since the completion of this report, some further calculations have been carried out. The purpose of this addendum is to describe briefly the motivation and results of this work.

The emphasis in the calculations to be described here is placed on the use of the OGO-6 model for specifying the background gas density and temperature. Since the helium density is an integral part of the OGO-6 model, the results of the theoretical calculations under specific solar/geophysical conditions can be compared directly with the He density given in the OGO-6 model. In contrast with the CIRA (1972) model, the OGO-6 model extends downwards from 450 km (where the data were taken) to the 120 km level. Since this lowest altitude is above the turbopause (which is to be found at 105-110 km), no effects on the He density of different (constant) values of the eddy diffusivity are to be expected. On the other hand, as will be seen shortly, this position of the lower boundary, coupled with the homogeneous boundary conditions of the theoretical model, leads to relatively unrealistic results.

The calculations were carried out in exactly the same manner as that described previously, except that the lower boundary was raised to 120 km. As in the eariler results, a substantial winter enhancement of helium was predicted at all altitudes. At a given altitude, the "bulge ratio," the ratio of global maximum to global minimum He density, increases with increasing $F_{10.7}$, as was also found in the calculations using the CIRA (1972) model. Furthermore, for a given value of $F_{10.7}$, the bulge ratio decreases with altitude above ~ 200 km, reflecting the effects of exospheric transport. Both of these qualitative features are also found in the mass-spectrometer data taken by the OGO-6, ESRO-4 and AE-C satellites.

However, quantitative comparison of the results of the theoretical model with the satellite data shows considerable discrepancies, which we attribute to the difference in the treatment of the 120 km boundary. The accompanying figure (Fig. 16) shows the bulge ratio as a function of altitude for two values of $F_{10.7}$: 100 (for which the ESRO-4 model is most applicable) and 140 (for which the OGO-6 model is most applicable). Comparison of the results of the theoretical model with the measured bulge ratios shows that the magnitude of the bulge ratio is underestimated in the theoretical model results. Since the 120 km level is considered to be characterized by constant He density (i.e., a bulge ratio of 1.0), the bulge ratio is artificially low at low thermospheric altitudes. The OGO-6 model shows a bulge ratio continuing to increase with decreasing altitude down to 120 km. In addition, the horizontal transport, which is responsible for the winter helium bulge, is forced to vanish at the 120 km level in this model. Therefore, although the bulge ratio in the theoretical model rises rapidly above the 120 km level, the wind field may be under-estimated in the 120-150 km region, and is therefore incapable of transporting

44

the wind field may be underestimated in the 120-150 km region, and is therefore incapable of transporting enough He from the summer to the winter hemisphere to bring the theoretical and empirical models into agreement at higher altitudes (where the measurements were made).

The difficulty arising from the placement of the boundary at 120 km is equivalent to an incorrect specification of the He density distribution at 120 km in the theoretical model. Although some investigators have taken this to imply a globally-varying value of the eddy diffusion coefficient, we feel that a correct description of the temperature and background density distributions below 120 km, and the use of that description in the theoretical model, could lead to a more realistic treatment of the global He variations. We hope to investigate such considerations in the future.

Figure 1. Horizontal wind field at June solstice for $F_{10.7} = 140$ x 10^{-22} w/m^2 - Hz, $K_p = 3$.

      a. 95 km altitude

      b. 118 km altitude

      c. 155 km altitude

      d. 206 km altitude

      e. 263 km altitude

      f. 320 km altitude

Figure 2. Horizontal wind field at June solstice for $F_{10.7} = 70$ x 10^{-22} w/m^2 - Hz, $K_p = 3$.

      a. 118 km altitude

      b. 206 km altitude

      c. 263 km altitude

      d. 320 km altitude

Alt → Symbol ↓	95	118	155	206	263	320	380	430	470	490
0	-5.6	-45.	-160.	-280.	-480.	-640.	-800.	-800.	-1200.	-1800.
6	-4.9	-40.	-140.	-240.	-420.	-560.	-700.	-600.	-1000.	-1500.
13	-4.2	-35.	-120.	-200.	-360.	-480.	-600.	-400.	-800.	-1200.
20	-3.5	-30.	-100.	-160.	-300.	-400.	-500.	-200.	-600.	-900.
26	-2.8	-25.	-80.	-120.	-240.	-320.	-400.	0.	-400.	-600.
33	-2.1	-20.	-60.	-80.	-180.	-240.	-300.	200.	-200.	-300.
40	-1.4	-15.	-40.	-40.	-120.	-160.	-200.	400.	0.	0
46	-0.7	-10.	-20.	0.	-60.	-80.	-100.	600.	200.	300.
53	0.	-5.	0.	40.	0.	0.	0.	800.	400.	600.
60	0.7	0.	20.	80.	60.	80.	100.	1000.	600.	900.
66	1.4	5.	40.	120.	120.	160.	200.	1200.	800.	1200.
73	2.1	10.	60.	160.	180.	240.	300.	1400.	1000.	1500.
80	2.8	15.	80.	200.	240.	320.	400.	1600.	1200.	1800.
87	3.5	20.	100.	240.	300.	400.	500.	1800.	1400.	2100.
93	4.2	25.	120.	280.	360.	480.	600.	2000.	1600.	2400.

Figure 3. Base gas vertical velocity w at selected altitudes for F 10.7 = 140 x 10^{-22} w/m^2 - Hz, K_p = 3. The following table gives the values of w in cm/sec corresponding to contour symbols which appear on the figures.

47

Alt→ Symbol↓	95	118	155	206	263	320	380	430	470	490
0	-2.4	-21.	-100.	-210.	-350.	-490.	-630.	-1000.	-1400.	-1800.
6	-2.0	-18.	-80.	-180.	-300.	-420.	-540.	-800.	-1200.	-1500.
13	-1.6	-15.	-60.	-150.	-250.	-350.	-450.	-600.	-1000.	-1200.
20	-1.2	-12.	-40.	-120.	-200.	-280.	-360.	-400.	-800.	-900.
26	-0.8	-9.	-20.	-90.	-150.	-210.	-270.	-200.	-600.	-600.
33	-0.4	-6.	0.	-60.	-100.	-140.	-180.	0.	-400.	-300.
40	0.0	-3.	20.	-30.	-50.	-70.	-90.	200.	-200.	0.
46	0.4	0.	40.	0.	0.	0.	0.	400.	0.	300.
53	0.8	3.	60.	30.	50.	70.	90.	600.	200.	600.
60	1.2	6.	80.	60.	100.	140.	180.	800.	400.	900.
66	1.6	9.	100.	90.	150.	210.	270.	1000.	600.	1200.
73	2.0	12.	120.	120.	200.	280.	360.	1200.	800.	1500.
80	2.4	15.	140.	150.	250.	350.	450.	1400.	1000.	1800.
87	2.8	18.	160.	180.	300.	420.	540.	1600.	1200.	2100.
93	3.2	21.	180.	210.	350.	490.	630.	1800.	1400.	2400.

Figure 4. Base gas vertical velocity w at selected altitudes for $F_{10.7}$ = 70 x 10^{-22} w/m^2 - Hz, K_p = 3. The following table gives the values of w in cm/sec corresponding to contour symbols which appear on the figures.

48

Figure 5. Vertical distributions of He under hydrostatic and non-hydrostatic ("dynamic") conditions. The calculations were carried out with $K = 10^7$ cm^2/sec using the CIRA (1972) model with $F_{10.7} = 140 \times 10^{-22}$ w/m^2 - Hz, Kp = 3. The hydrostatic curves represent the positions of global maximum and minimum exospheric temperature, corresponding to global He maximum and minimum. The dynamic curves also correspond to global maximum and minimum, which occur (for June solstice) at high winter latitude and the summer pole, respectively.

Figure 6. Contours of constant values of $\log_{10} (\rho_{He}, g/cm^3)$ at June solstice for $F_{10.7} = 140 \times 10^{-22}$ w/m^2 - Hz, $K_p = 3$, $K = 3 \times 10^6$ cm^2/sec.

     a. 95 km altitude
     b. 118 km altitude
     c. 155 km altitude
     d. 206 km altitude
     e. 263 km altitude
     f. 320 km altitude
     g. 380 km altitude
     h. 430 km altitude
     i. 470 km altitude
     j. 490 km altitude

Figure 7. Contours of constant values of $\log_{10} (\rho_{He}, g/cm^3)$ at June solstice for $F_{10.7} = 140 \times 10^{-22}$ w/m^2 - Hz, $K_p = 3$, $K = 6 \times 10^6$ cm^2/sec.

     a. 95 km altitude
     b. 118 km altitude
     c. 155 km altitude
     d. 206 km altitude

Figure 8. Contours of constant values of $\log_{10}(\rho_{He}, \text{ g/cm}^3)$ at June solstice for $F_{10.7} = 100 \text{ w/m}^2$ - Hz, $K_p = 3$, $K = 10^7 \text{ cm}^2/\text{sec}$.

Figure 9. Contours of constant values of $\log_{10}(\rho_{He}, \text{ g/cm}^3)$ at June solstice for $F_{10.7} = 70 \times 10^{-22} \text{ w/m}^2$ - Hz, $K_p = 3$, $K = 10^7 \text{ cm}^2/\text{sec}$.

Figure 10. Comparison of the global ratio of maximum to minimum He density at fixed altitudes as predicted by the model with that derived from mass-spectrometer data taken on various satellites. The variation of this ratio with solar activity, as measured by the flux at 10.7 cm in units of 10^{-22} w/m^2 - Hz, is shown.

Figure 11. Vertical distributions of A under hydrostatic and non-hydrostatic ("dynamic") conditions. The calculations were carried out with $K = 10^7$ cm^2/sec using the CIRA (1972) model with $F_{10.7} = 100 \times 10^{-22}$ w/m^2 - Hz, $K_p = 3$. The hydrostatic curves represent the positions of maximum and minimum exospheric temperature, corresponding to global A maximum and minimum. The dynamic curves also correspond to global maximum and minimum.

Figure 12. Contours of constant values of $\log_{10}$ (A, g/cm^3) at June solstice for $F_{10.7} = 100 \times 10^{-22}$ w/m^2 - Hz, $K_p = 3$, $K = 10^7$ cm^2/sec.

      a. 95 km altitude
      b. 155 km altitude
      c. 206 km altitude
      d. 263 km altitude
      e. 320 km altitude
      f. 430 km altitude

Figure 13. Bates and Jacchia (CIRA, 1972) vertical temperature profiles for two values of the exospheric temperature T_∞.

Figure 14. Contours of O concentration (in units of $10^{11}/cm^3$) at
120 km from the extrapolation of the OGO-6 model values
with Jacchia temperature profiles (a) June solstice (b)
September equinox.

Figure 15. Contours of the N_2 concentration (in units of $10^{11}/cm^3$)
at 120 km from the extrapolation of the OGO-6 model values
with Jacchia temperature profiles (a) June solstice (b)
September equinox.

Figure 16. Comparison of the global ratio of maximum to minimum
He density as a function of altitude as predicted by the
theoretical model (using the OGO-6 model to specify
background gas characteristics) and as measured by
satellite-borne mass spectrometers. The variation of this
ratio with solar activity, as measured by the flux at
10.7 cm in units of 10^{-22} w/m^2-Hz, is shown.

WIND FIELD AT ALTITUDE 95
JUNE SOLSTICE

$F_{10.7} = 140$ 18 m/sec

LATITUDE

90
60
30
0
-30
-60
-90

12 14 16 18 20 22 0 2 4 6 8 10

LOCAL TIME (hr)

WIND FIELD AT ALTITUDE 118
JUNE SOLSTICE

$F_{10.7} = 140$

75 m/sec

LATITUDE

LOCAL TIME (hr)

Fig. 1b

WIND FIELD AT ALTITUDE 155
JUNE SOLSTICE

$F_{10.7} = 140$ 130 m/sec

LATITUDE

LOCAL TIME (hr)

Fig. 1c

WIND FIELD AT ALTITUDE 206
JUNE SOLSTICE

Fig. 1d

WIND FIELD AT ALTITUDE 263
JUNE SOLSTICE

$F_{10.7} = 140$ 200 m/sec

WIND FIELD AT ALTITUDE 320
JUNE SOLSTICE

$F_{10.7} = 140$ 210 m/sec

WIND FIELD AT ALTITUDE 118
JUNE SOLSTICE

Fig. 2a

WIND FIELD AT ALTITUDE 206
JUNE SOLSTICE

$F_{10.7} = 70$ 130 m/sec

LATITUDE

LOCAL TIME (hr)

Fig. 2b

WIND FIELD AT ALTITUDE 263
JUNE SOLSTICE

$F_{10.7} = 70$ 168 m/sec

LATITUDE

90
60
30
0
-30
-60
-90

LOCAL TIME (hr)

12 14 16 18 20 22 0 2 4 6 8 10

Fig. 2c

WIND FIELD AT ALTITUDE 320
JUNE SOLSTICE

$F_{10.7} = 70$ 180 m/sec

Fig. 2d

CONTOURS OF BASE GAS RADIAL WIND AT ALTITUDE 95

JUNE SOLSTICE

$F_{10.7} = 140$

Fig. 3a

CONTOURS OF BASE GAS RADIAL WIND AT ALTITUDE 118

JUNE SOLSTICE

$F_{10.7} = 140$

CONTOURS OF BASE GAS RADIAL WIND AT ALTITUDE 155

JUNE SOLSTICE

$F_{10.7} = 140$

LOCAL TIME

CONTOURS OF BASE GAS RADIAL WIND AT ALTITUDE 206

JUNE SOLSTICE

$F_{10.7} = 140$

Fig. 3d

CONTOURS OF BASE GAS RADIAL WIND AT ALTITUDE 263

JUNE SOLSTICE

$F_{10.7} = 140$

Fig. 3e

CONTOURS OF BASE GAS RADIAL WIND AT ALTITUDE 320

JUNE SOLSTICE

$F_{10.7} = 140$

CONTOURS OF BASE GAS RADIAL WIND AT ALTITUDE 380

JUNE SOLSTICE

$$F_{10.7} = 140$$

CONTOURS OF BASE GAS RADIAL WIND AT ALTITUDE 430

JUNE SOLSTICE

$F_{10.7} = 140$

CONTOURS OF BASE GAS RADIAL WIND AT ALTITUDE 470

JUNE SOLSTICE

$F_{10.7} = 140$

Fig. 3i

CONTOURS OF BASE GAS RADIAL WIND AT ALTITUDE 490

JUNE SOLSTICE

$$F_{10.7} = 140$$

LOCAL TIME

CONTOURS OF BASE GAS RADIAL WIND AT ALTITUDE 95

JUNE SOLSTICE

$F_{10.7} = 70$

CONTOURS OF BASE GAS RADIAL WIND AT ALTITUDE 118

JUNE SOLSTICE

$F10.7 = 70$

Fig. 4b

CONTOURS OF BASE GAS RADIAL WIND AT ALTITUDE 155

JUNE SOLSTICE

$F_{10.7} = 70$

Fig. 4c

CONTOURS OF BASE GAS RADIAL WIND AT ALTITUDE 206

JUNE SOLSTICE

$F_{10.7} = 70$

CONTOURS OF BASE GAS RADIAL WIND AT ALTITUDE 263

JUNE SOLSTICE

$F_{10.7} = 70$

CONTOURS OF BASE GAS RADIAL WIND AT ALTITUDE 320

JUNE SOLSTICE

$F_{10.7} = 70$

Fig. 4f

CONTOURS OF BASE GAS RADIAL WIND AT ALTITUDE 380

JUNE SOLSTICE

$F_{10.7} = 70$

Fig. 4g

CONTOURS OF BASE GAS RADIAL WIND AT ALTITUDE 430

JUNE SOLSTICE

$F_{10.7} = 70$

Fig. 4h

CONTOURS OF BASE GAS RADIAL WIND AT ALTITUDE 470

JUNE SOLSTICE

$F_{10.7} = 70$

CONTOURS OF BASE GAS RADIAL WIND AT ALTITUDE 490
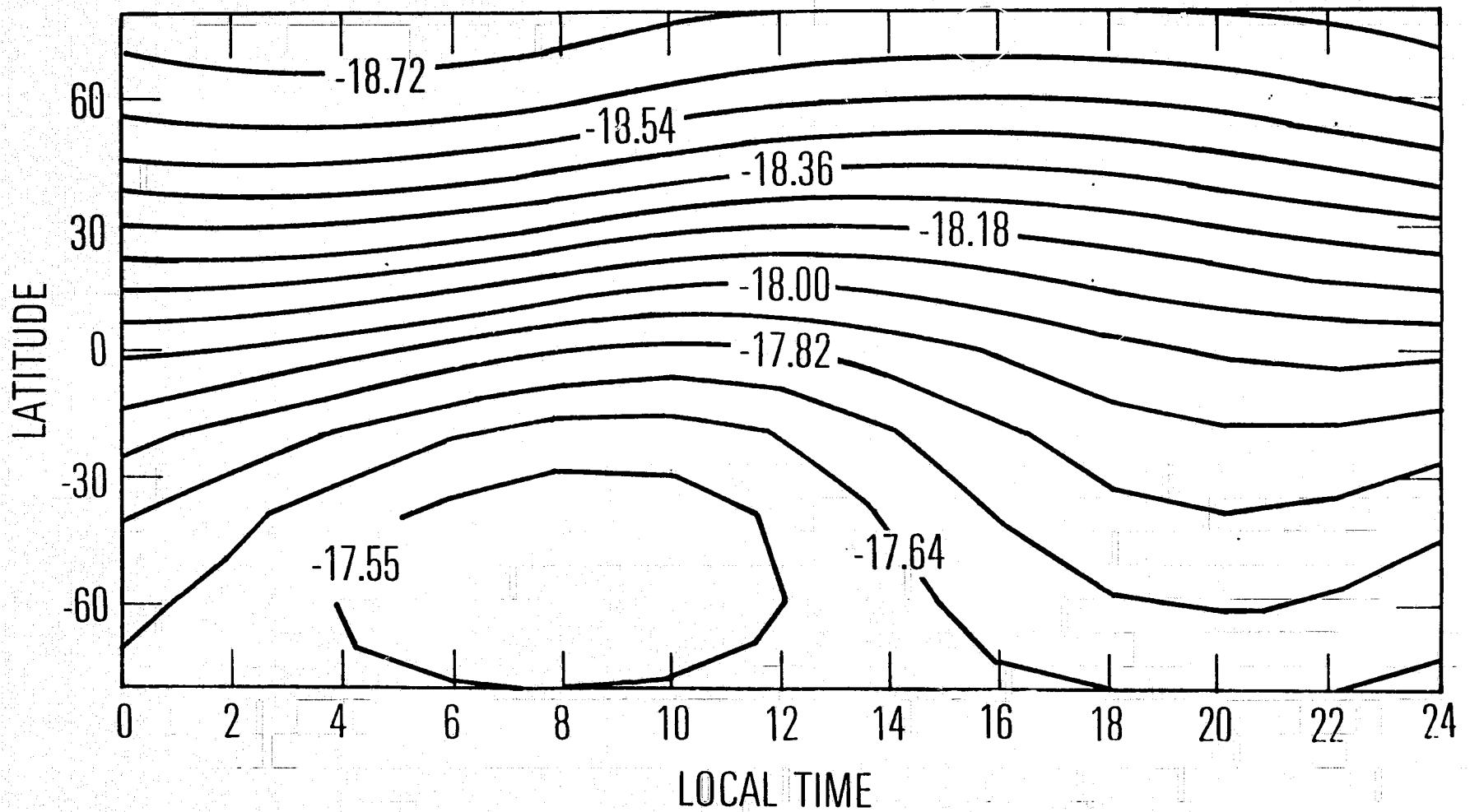
JUNE SOLSTICE

$$F_{10.7} = 70$$

Fig. 5

CONTOURS OF HELIUM DENSITY AT ALTITUDE 95
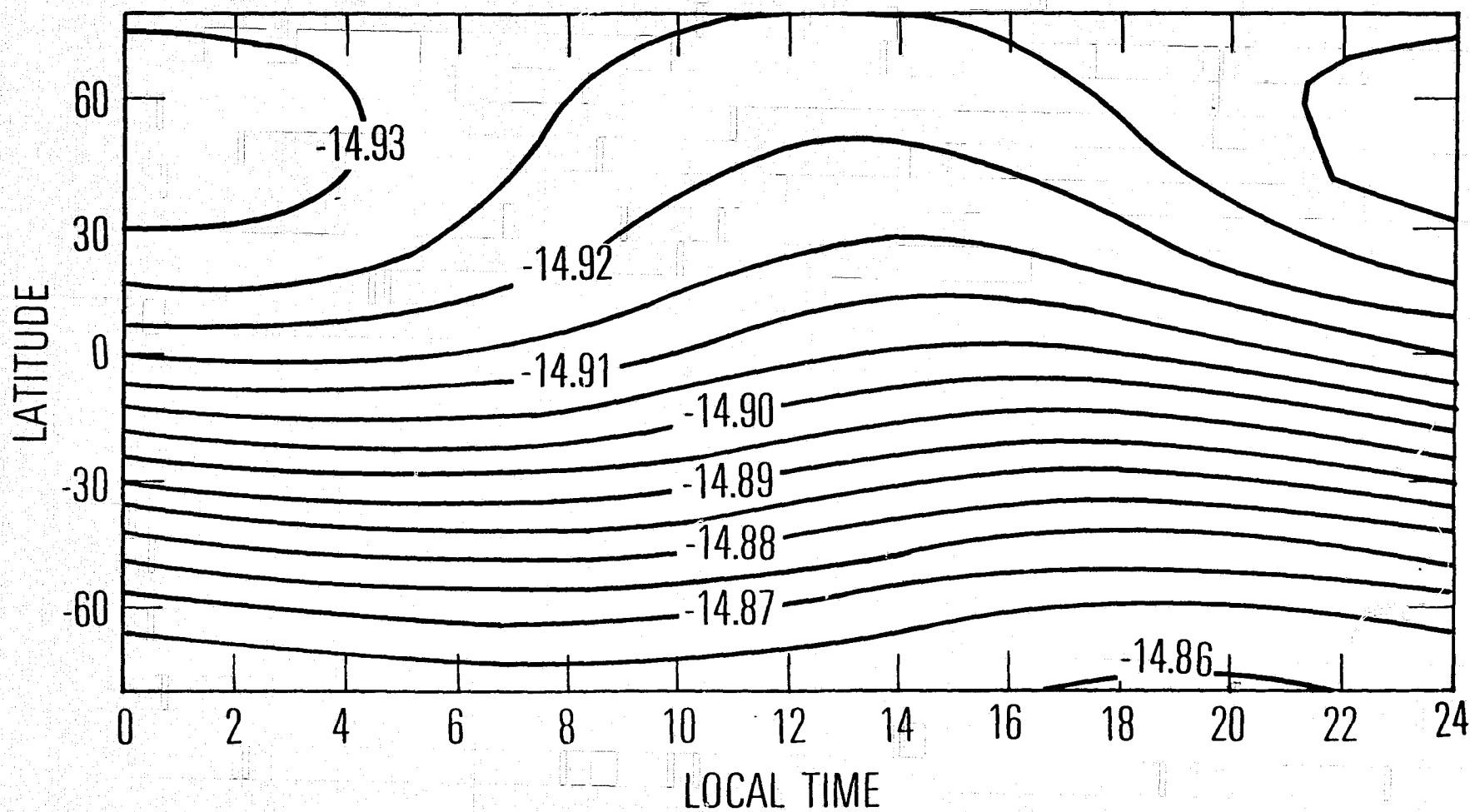JUNE SOLSTICE

$F_{10.7} = 140 \qquad K = 3 \times 10^6$

CONTOURS OF HELIUM DENSITY AT ALTITUDE 118
JUNE SOLSTICE

$F_{10.7} = 140$ $k = 3 \times 10^6$
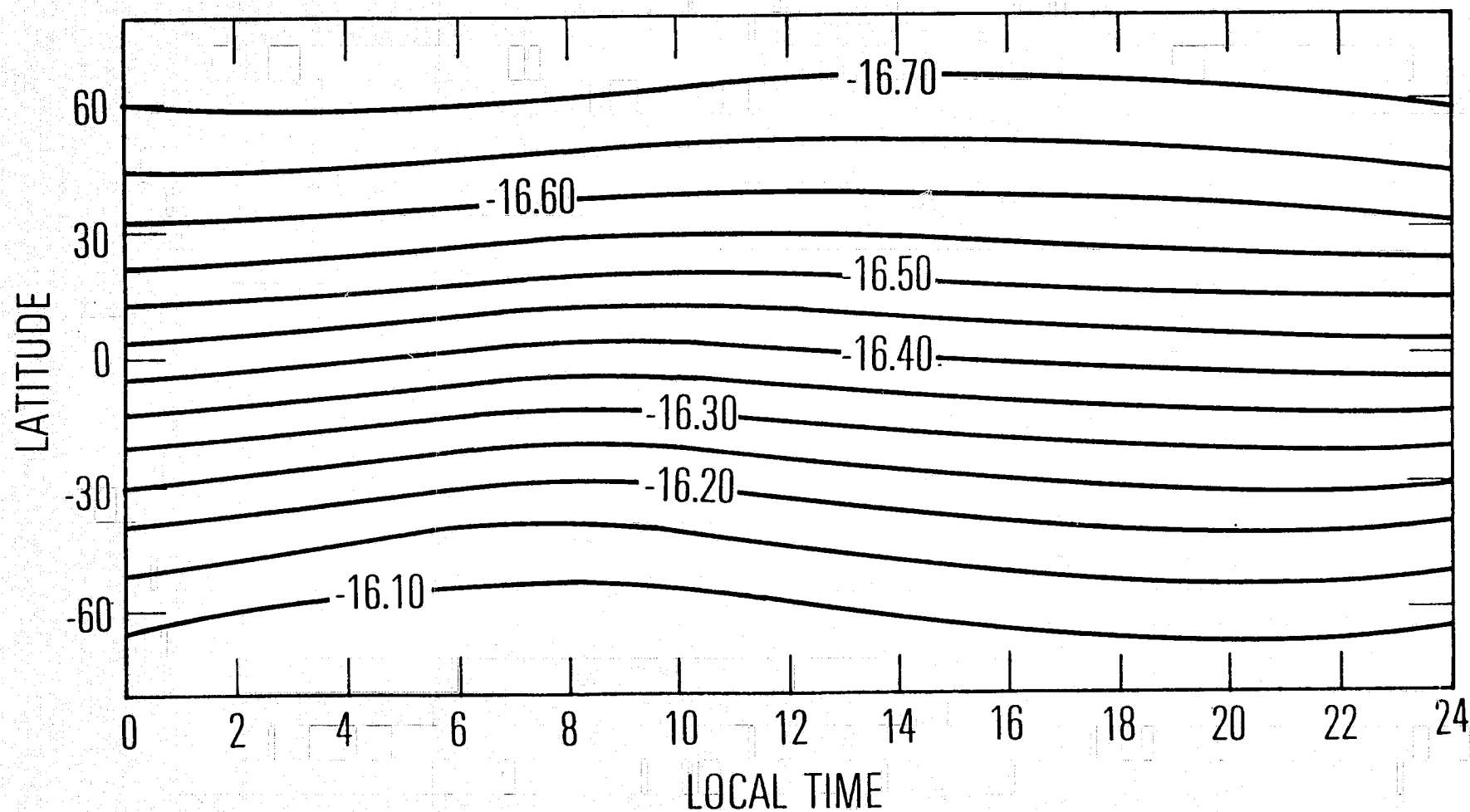
CONTOURS OF HELIUM DENSITY AT ALTITUDE 155
JUNE SOLSTICE

$F_{10.7} = 140$ $K = 3 \times 10^6$

Fig. 6c

CONTOURS OF HELIUM DENSITY AT ALTITUDE 206
JUNE SOLSTICE

$$F_{10.7} = 140 \qquad K = 3 \times 10^6$$

CONTOURS OF HELIUM DENSITY AT ALTITUDE 263
JUNE SOLSTICE

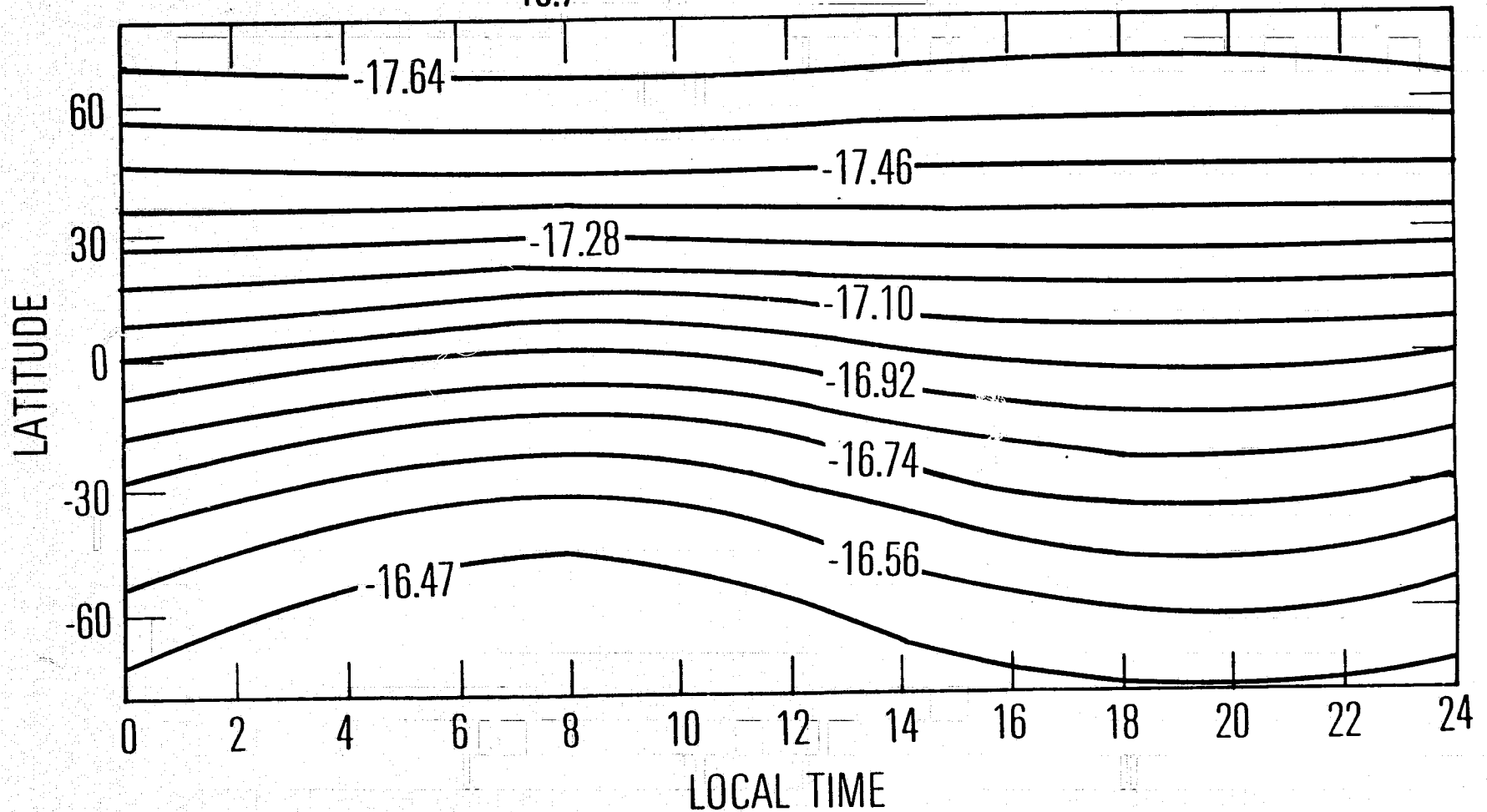$$F_{10.7} = 140 \qquad K = 3 \times 10^6$$

CONTOURS OF HELIUM DENSITY AT ALTITUDE 320
JUNE SOLSTICE

$F_{10.7} = 140$ $K = 3 \times 10^6$

CONTOURS OF HELIUM DENSITY AT ALTITUDE 380
JUNE SOLSTICE

$F_{10.7} = 140$ $K = 3 \times 10^6$

Fig. 6g

CONTOURS OF HELIUM DENSITY AT ALTITUDE 430
JUNE SOLSTICE

$$F_{10.7} = 140 \qquad K = 3 \times 10^6$$

CONTOURS OF HELIUM DENSITY AT ALTITUDE 470
JUNE SOLSTICE

$$F_{10.7} = 140 \qquad K = 3 \times 10^6$$

CONTOURS OF HELIUM DENSITY AT ALTITUDE 490
JUNE SOLSTICE

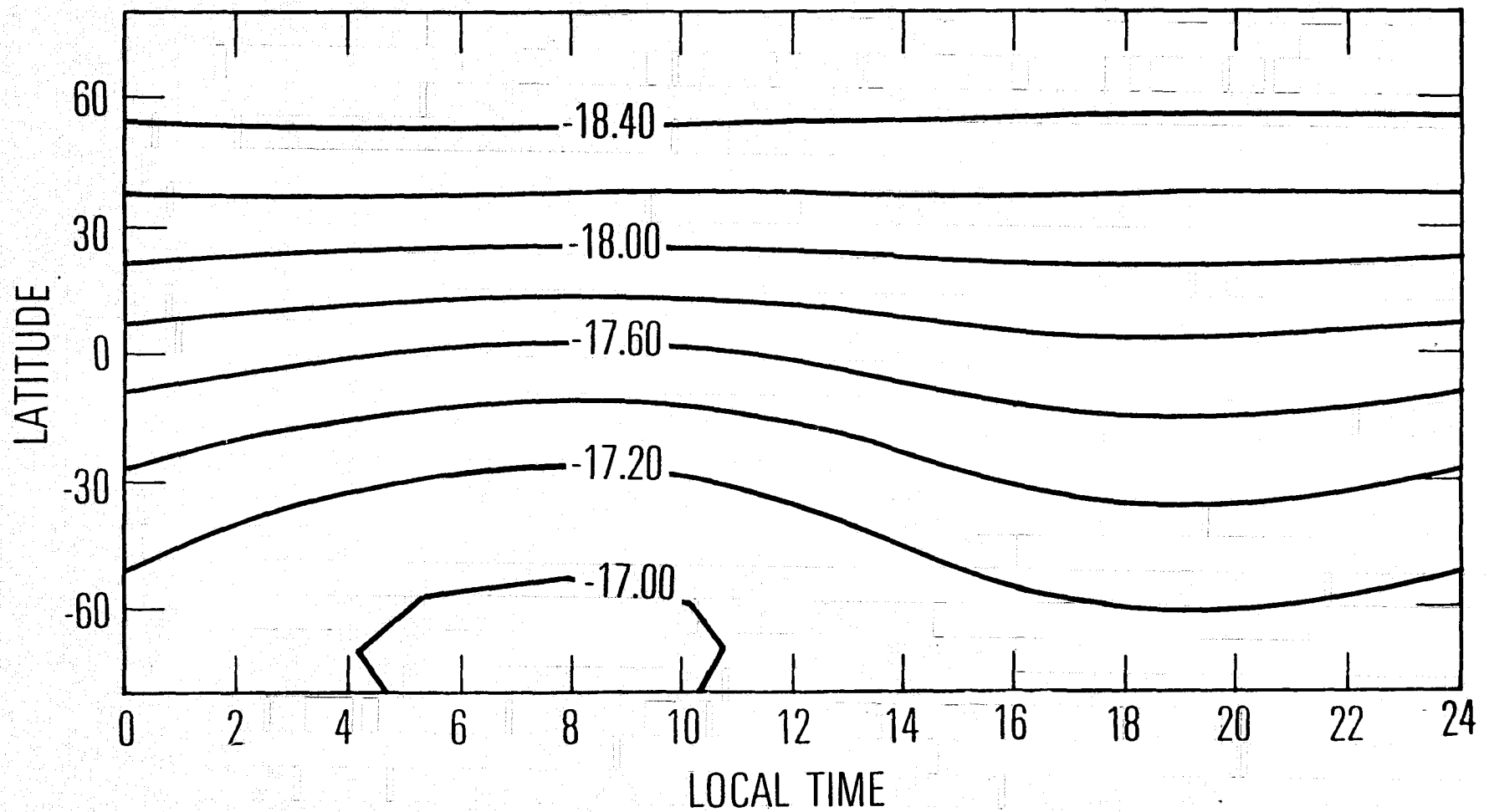$F_{10.7} = 140$ $K = 3 \times 10^6$

Fig. 6j

CONTOURS OF HELIUM DENSITY AT ALTITUDE 95
JUNE SOLSTICE

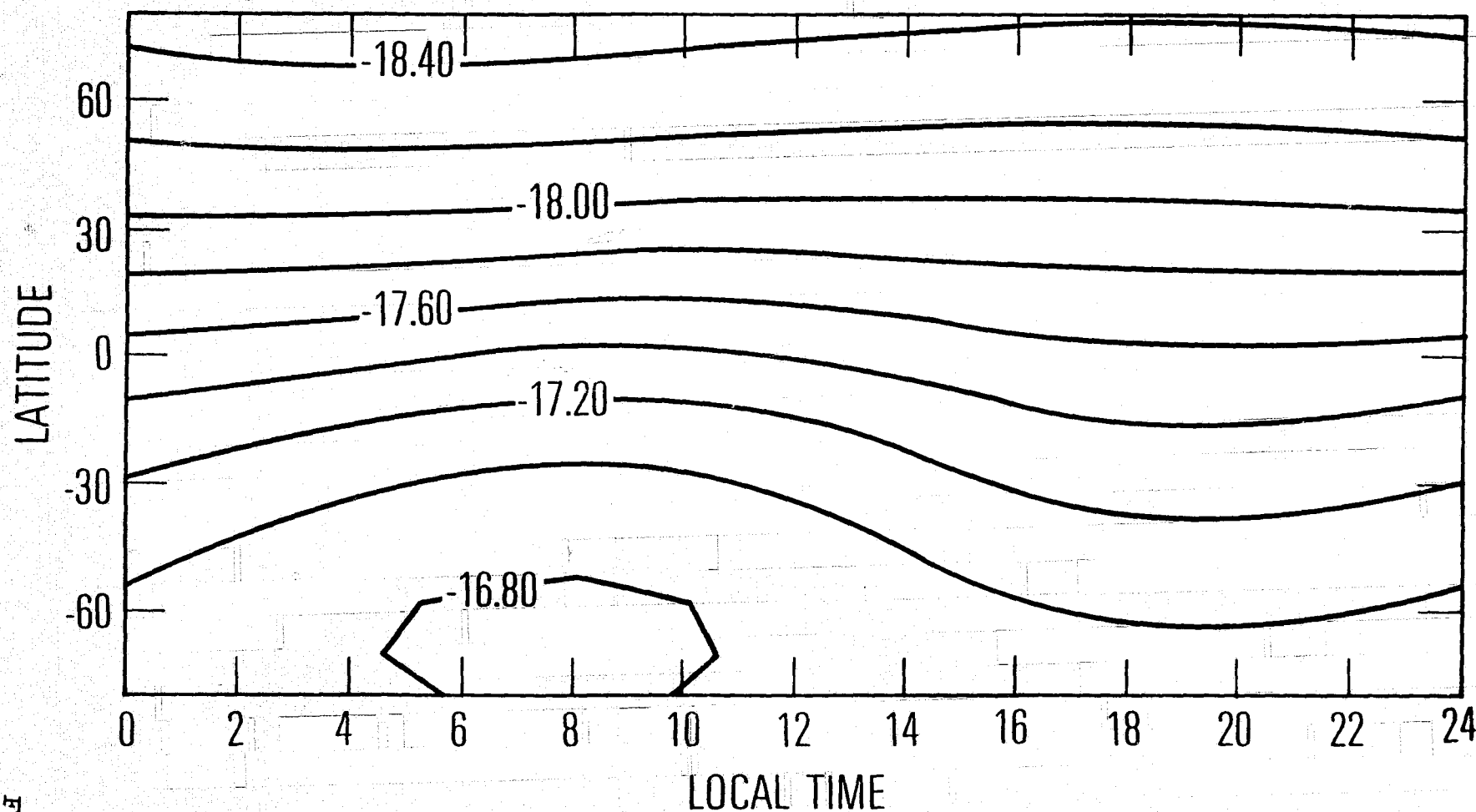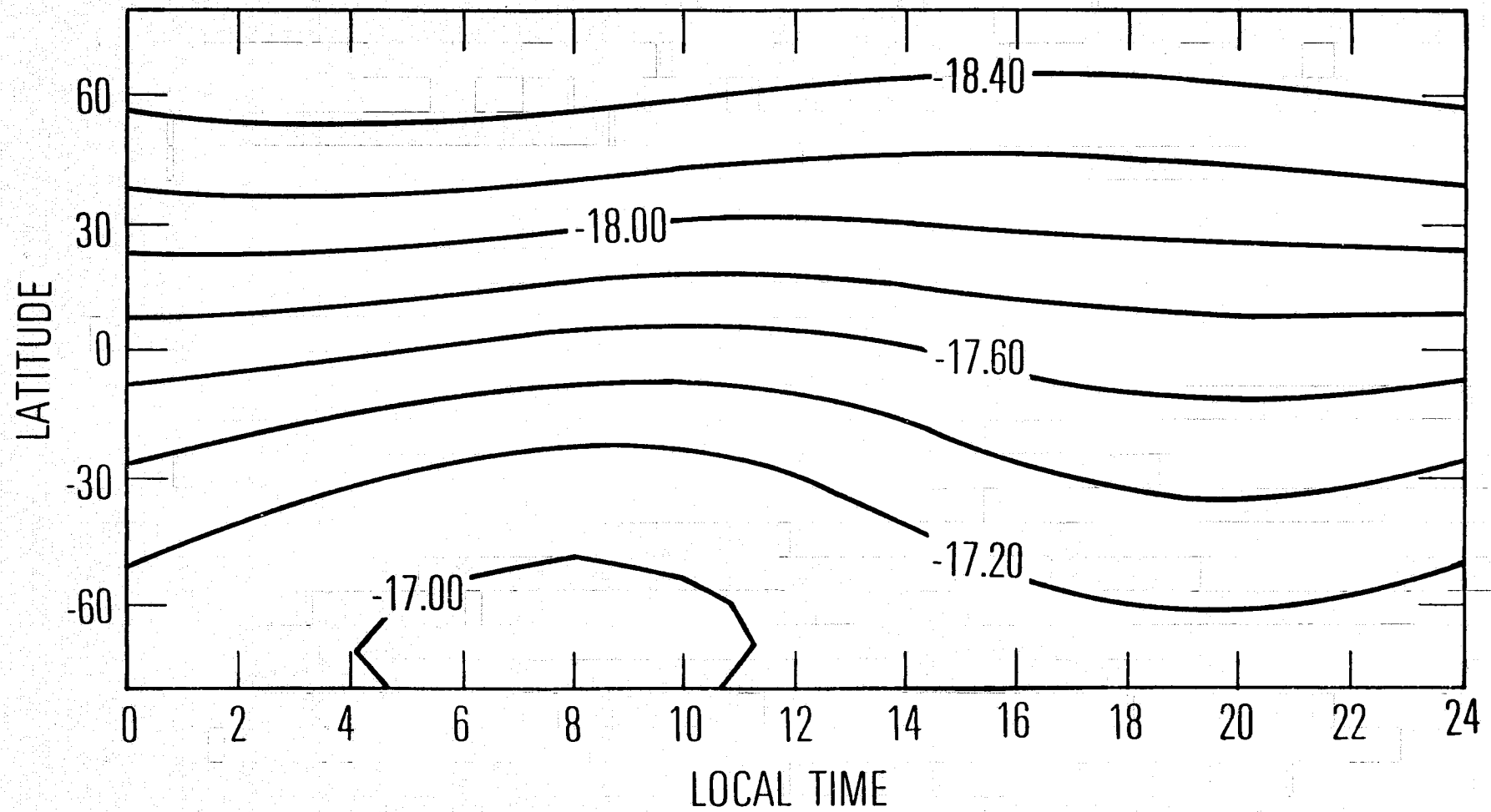$F_{10.7} = 140$ $K = 6 \times 10^6$

CONTOURS OF HELIUM DENSITY AT ALTITUDE 118
JUNE SOLSTICE
$F_{10.7} = 140$ $K = 6 \times 10^6$

CONTOURS OF HELIUM DENSITY AT ALTITUDE 155
JUNE SOLSTICE
$F_{10.7} = 140 \quad K = 6 \times 10^6$

Fig. 7c

CONTOURS OF HELIUM DENSITY AT ALTITUDE 206
JUNE SOLSTICE

$F_{10.7} = 140 \quad K = 6 \times 10^6$

CONTOURS OF HELIUM DENSITY AT ALTITUDE 263
JUNE SOLSTICE

$F_{10.7} = 140$ $K = 6 \times 10^6$

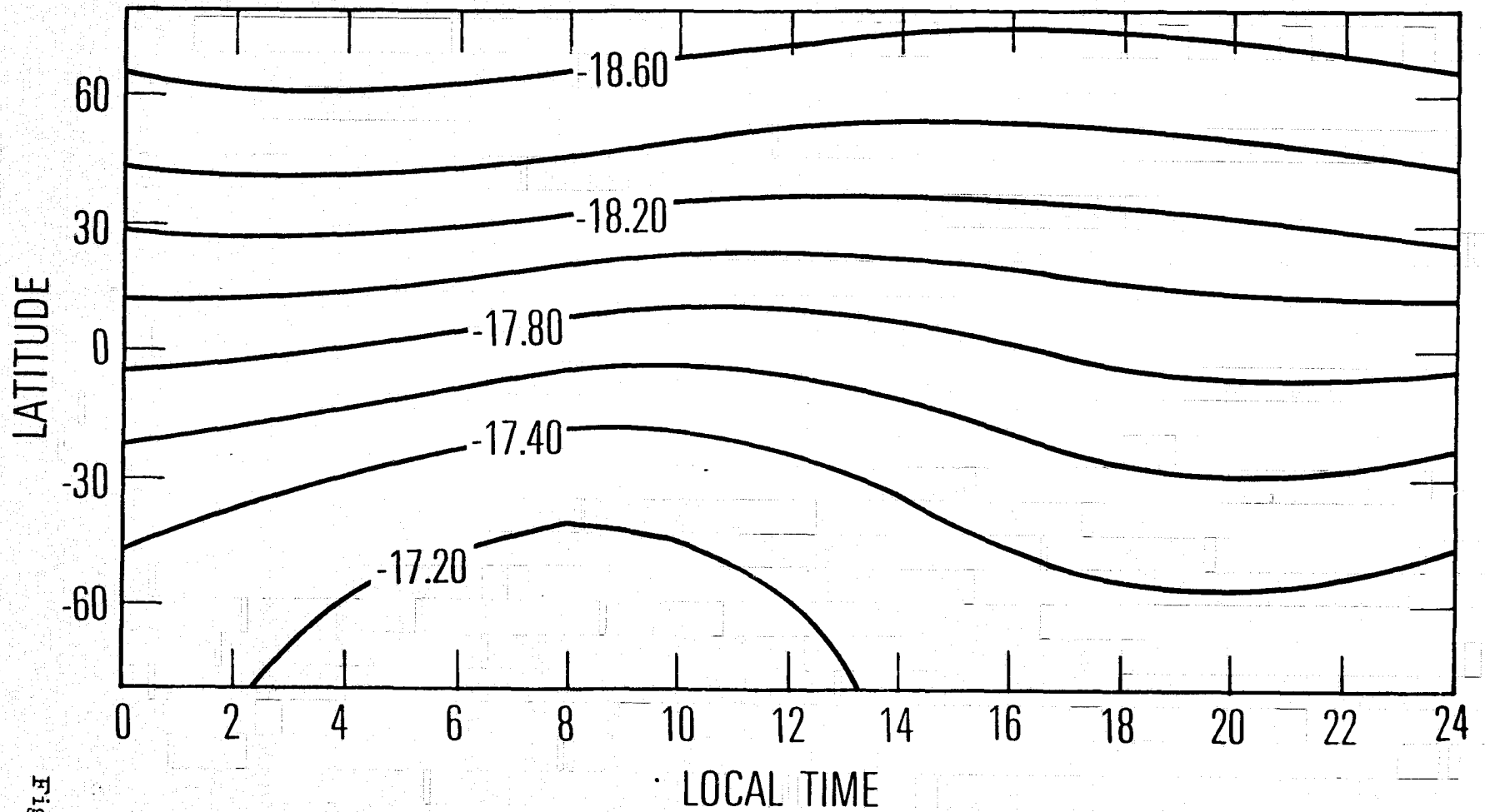# CONTOURS OF HELIUM DENSITY AT ALTITUDE 320
JUNE SOLSTICE

$F_{10.7} = 140$ $K = 6 \times 10^{6}$

LATITUDE

LOCAL TIME

-17.92
-17.78
-17.64
-17.50
-17.36
-17.22
-17.08

CONTOURS OF HELIUM DENSITY AT ALTITUDE 380
JUNE SOLSTICE
$F_{10.7} = 140 \quad K = 6 \times 10^6$

CONTOURS OF HELIUM DENSITY AT ALTITUDE 430
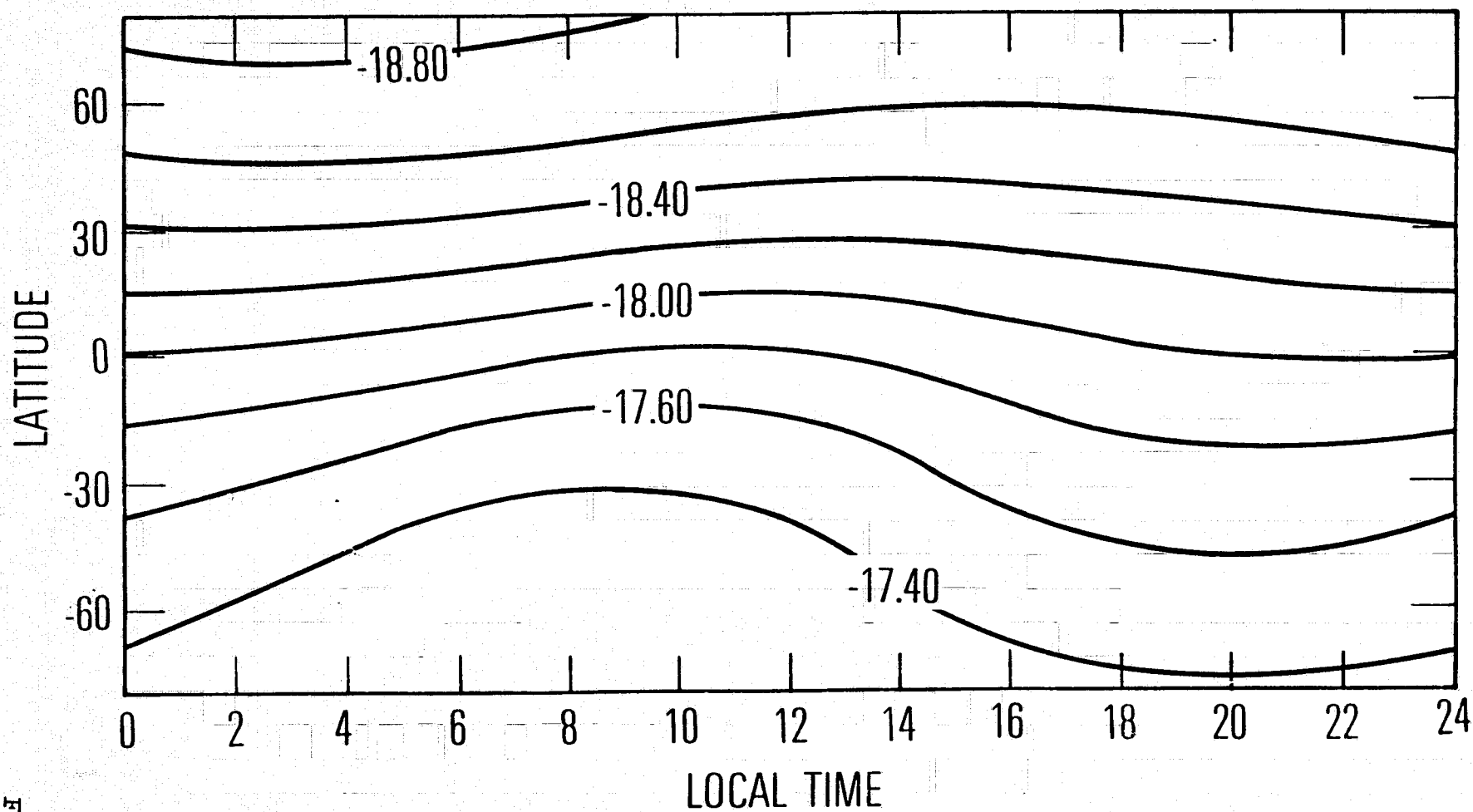
JUNE SOLSTICE

$F_{10.7} = 140 \quad K = 6 \times 10^6$

Fig. 7

CONTOURS OF HELIUM DENSITY AT ALTITUDE 470
JUNE SOLSTICE

$$F_{10.7} = 140 \qquad K = 6 \times 10^6$$

CONTOURS OF HELIUM DENSITY AT ALTITUDE 490
JUNE SOLSTICE
F10.7 = 140   K = 6 x 10^6

CONTOURS OF HELIUM DENSITY AT ALTITUDE 95
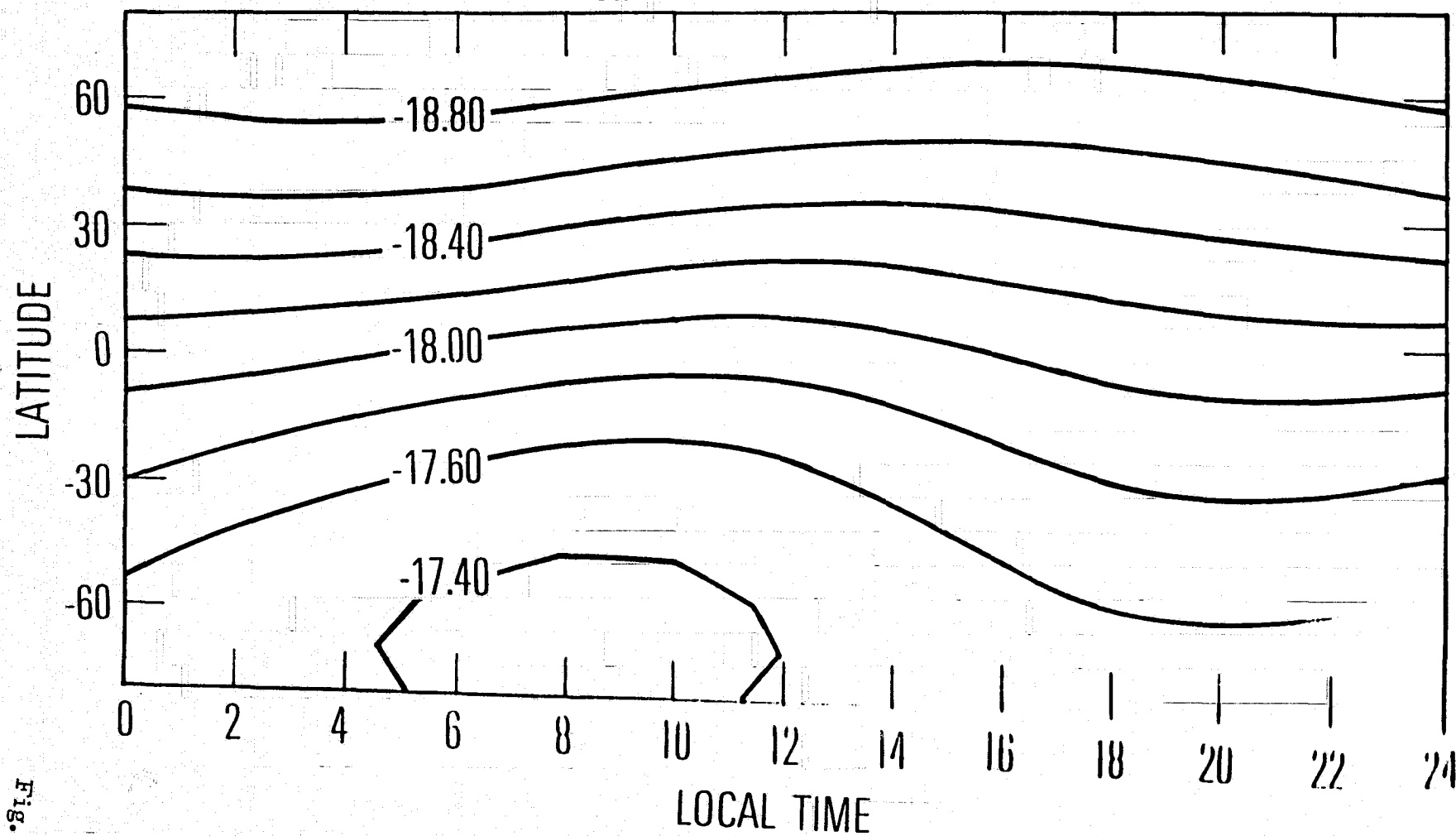JUNE SOLSTICE
$F_{10.7} = 100$ $K = 10^7$ cm^2/sec
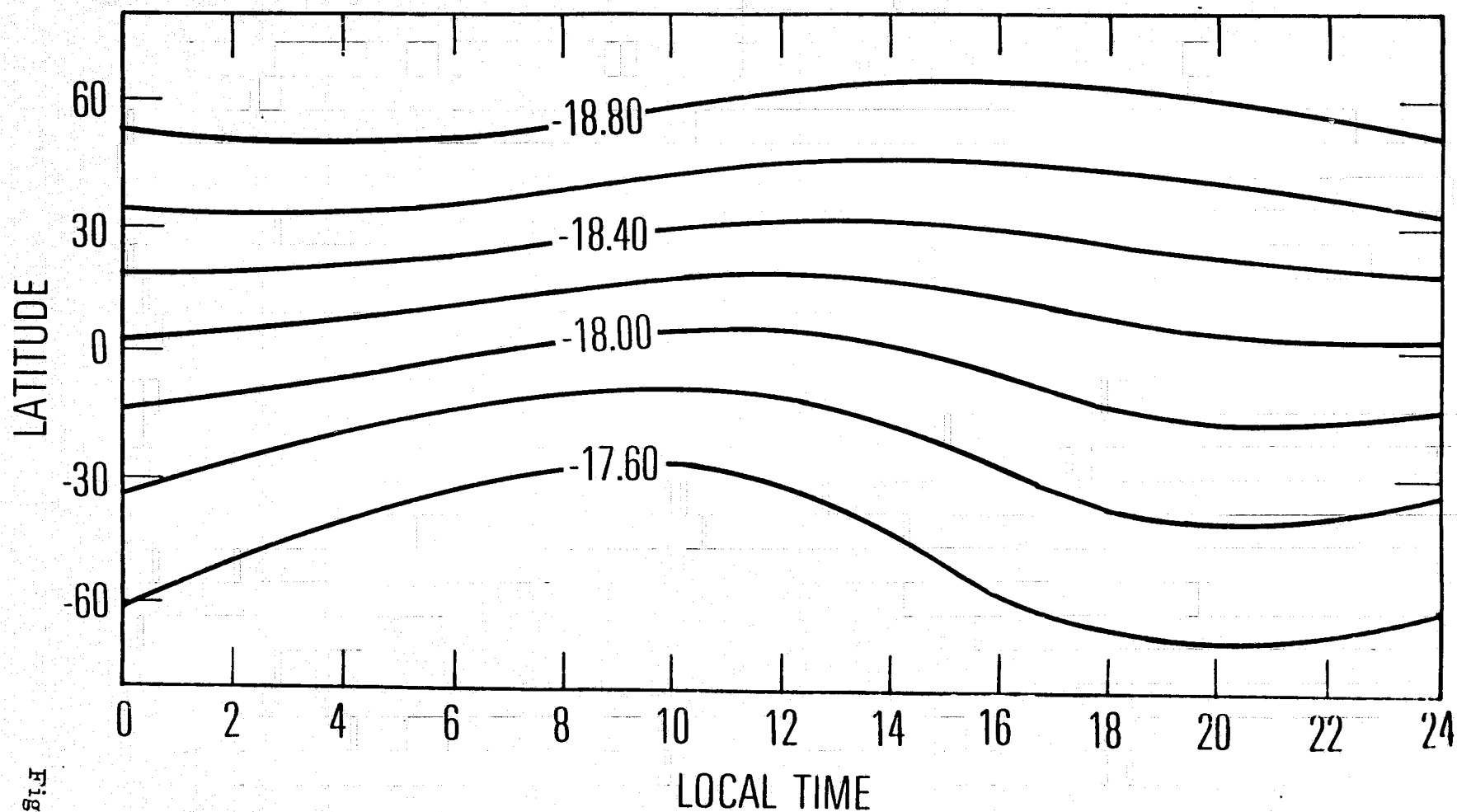
CONTOURS OF HELIUM DENSITY AT ALTITUDE 118
JUNE SOLSTICE
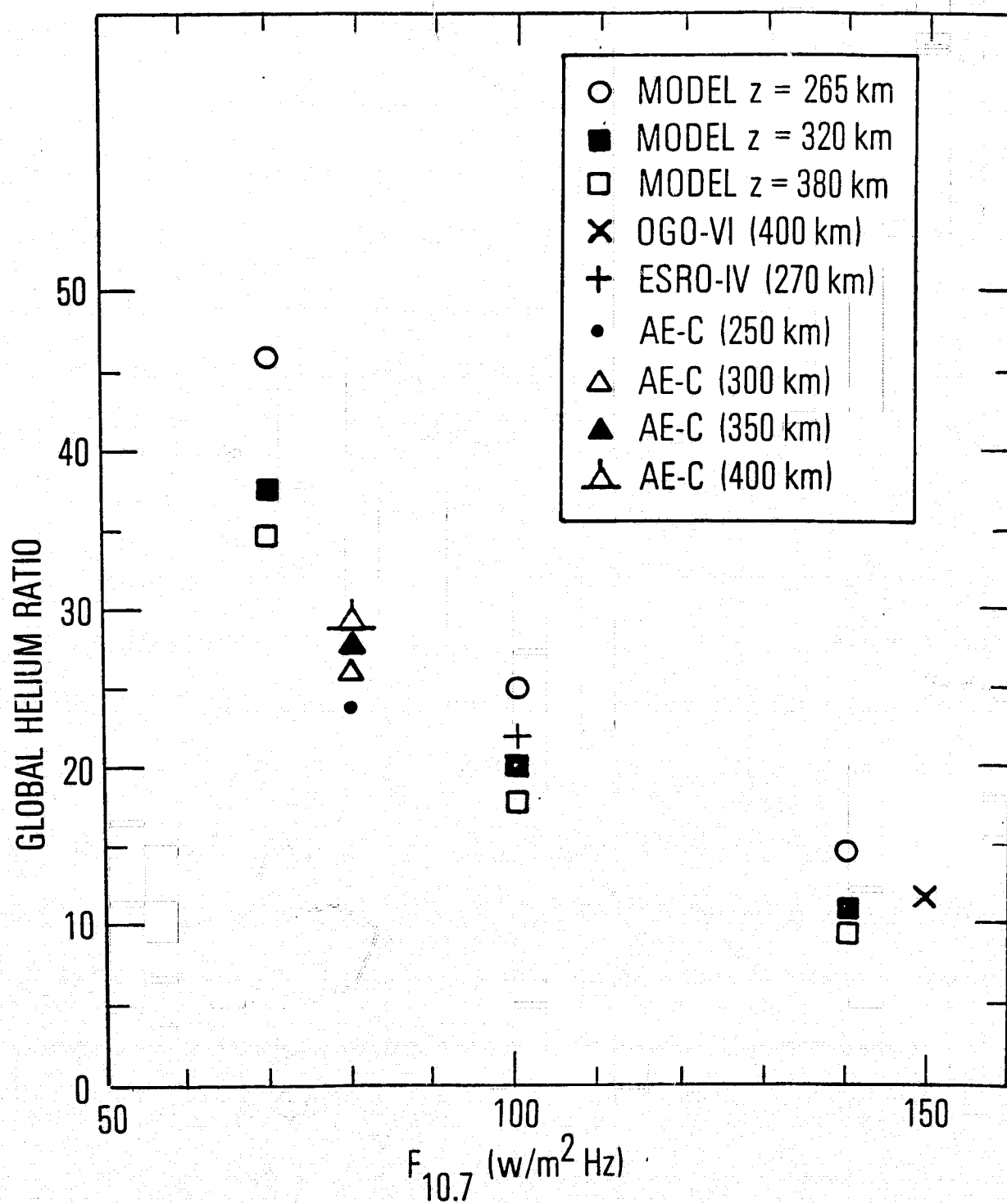$F_{10.7} = 100 \quad K = 10^7 \; cm^2/sec$

Fig. 8b

CONTOURS OF HELIUM DENSITY AT ALTITUDE 155

JUNE SOLSTICE

$F_{10.7} = 100$ $K = 10^7$ cm^2/sec

Fig. 8c

CONTOURS OF HELIUM DENSITY AT ALTITUDE 206

JUNE SOLSTICE

$F_{10.7} = 100$ $K = 10^7$ cm^2/sec

CONTOURS OF HELIUM DENSITY AT ALTITUDE 263
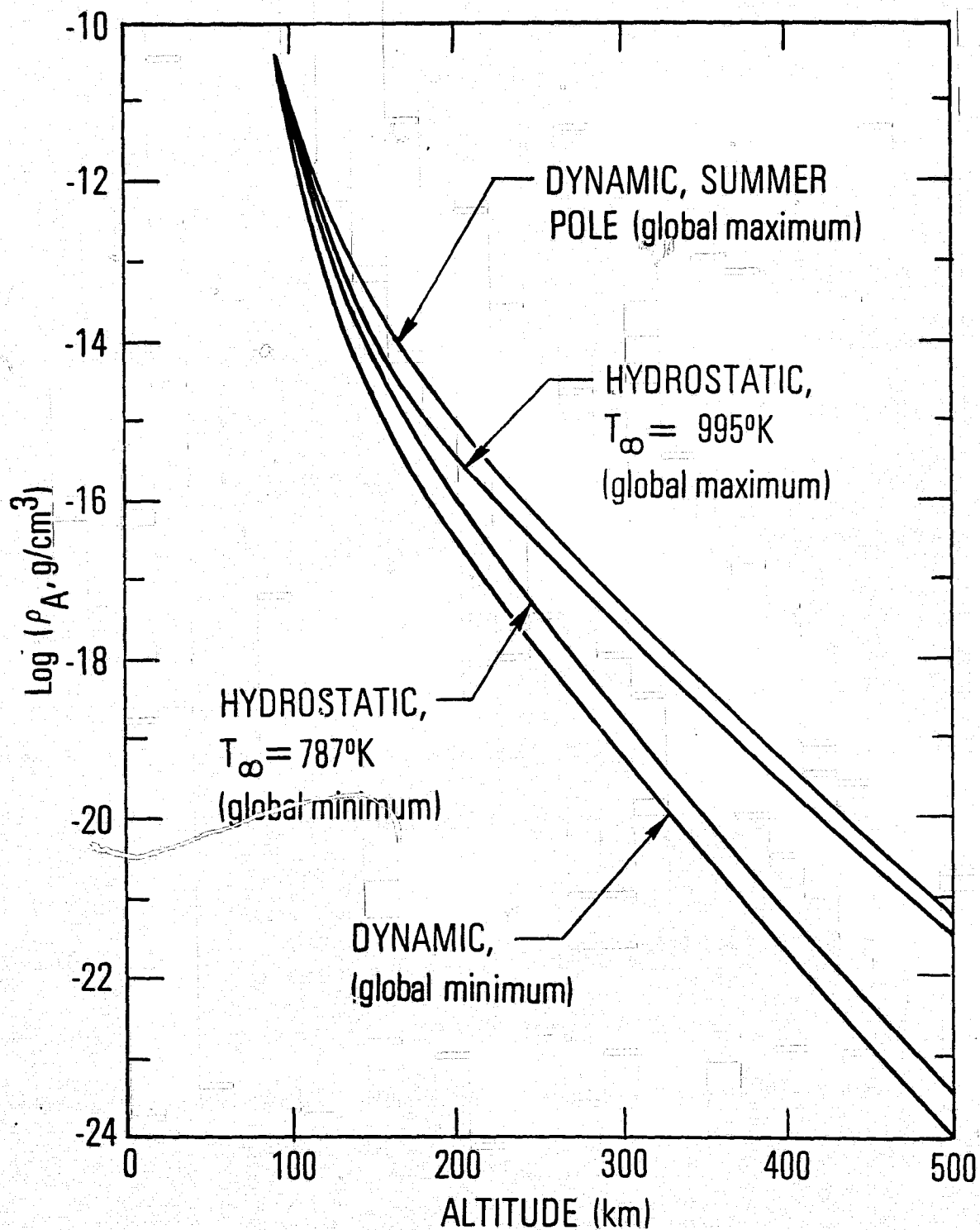
JUNE SOLSTICE

$F_{10.7} = 100 \quad K = 10^7 \ cm^2/sec$

CONTOURS OF HELIUM DENSITY AT ALTITUDE 320
JUNE SOLSTICE
$F_{10.7} = 100 \quad K = 10^7 \ cm^2/sec$

CONTOURS OF HELIUM DENSITY AT ALTITUDE 380
JUNE SOLSTICE
$F_{10.7} = 100 \quad K = 10^7 \text{ cm}^2/\text{sec}$

Fig. 8g

CONTOURS OF HELIUM DENSITY AT ALTITUDE 430

JUNE SOLSTICE

$F_{10.7} = 100 \quad K = 10^7 \ cm^2/sec$

CONTOURS OF HELIUM DENSITY AT ALTITUDE 470
JUNE SOLSTICE

$$F_{10.7} = 100 \quad K = 10^7 \ cm^2/sec$$

CONTOURS OF HELIUM DENSITY AT ALTITUDE 490

JUNE SOLSTICE

$F_{10.7} = 100 \quad K = 10^7 \ cm^2/sec$

CONTOURS OF HELIUM DENSITY AT ALTITUDE 95

JUNE SOLSTICE

$F_{10.7} = 70 \quad K = 10^7$

CONTOURS OF HELIUM DENSITY AT ALTITUDE 118 —
JUNE SOLSTICE

$F_{10.7} = 70$ $K = 10^7$

CONTOURS OF HELIUM DENSITY AT ALTITUDE 155
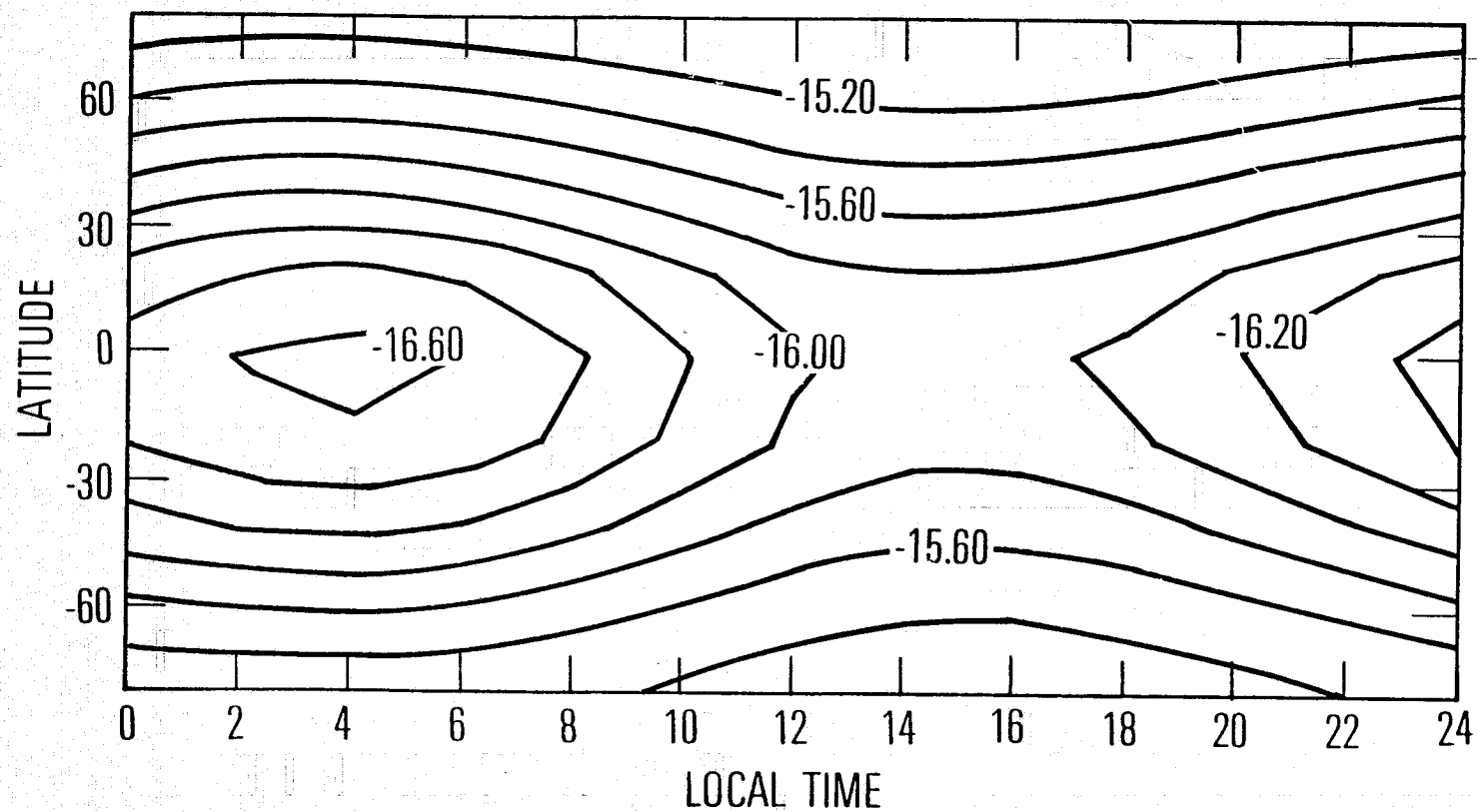JUNE SOLSTICE
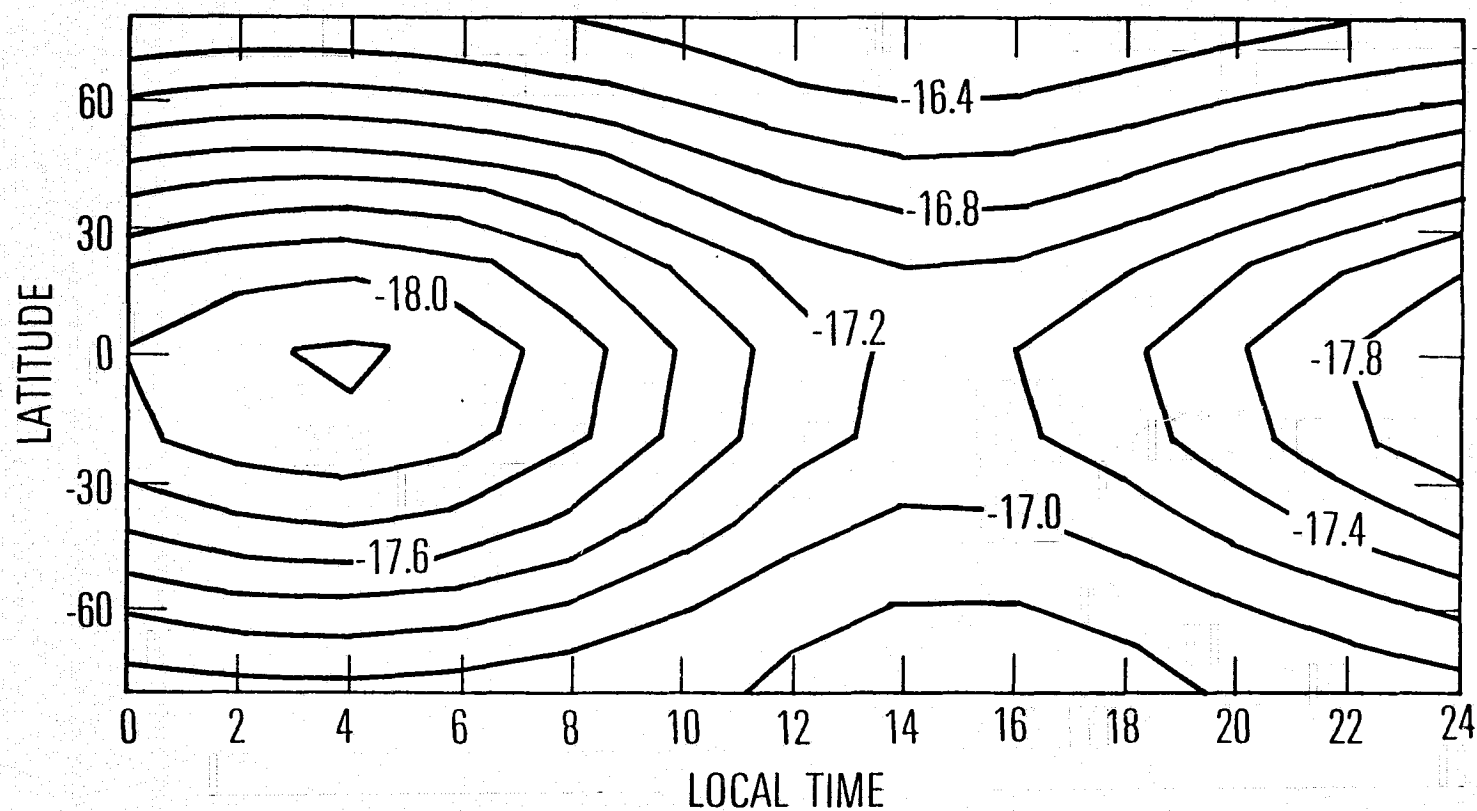$F_{10.7} = 70$ $K = 10^7$

Fig. 9c

CONTOURS OF HELIUM DENSITY AT ALTITUDE 206
JUNE SOLSTICE
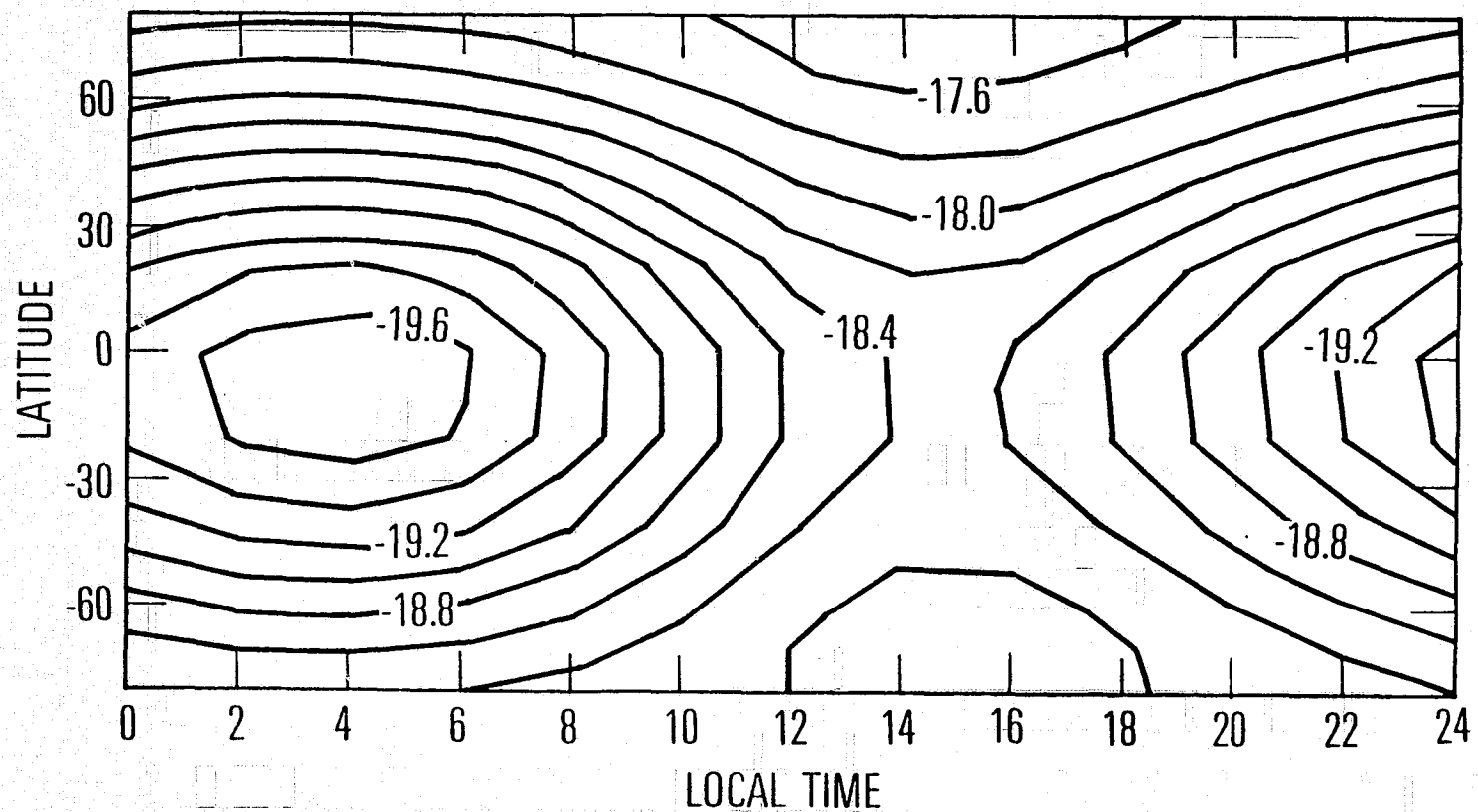$F_{10.7} = 70 \qquad K = 10^7$

CONTOURS OF HELIUM DENSITY AT ALTITUDE 263
JUNE SOLSTICE
$$F_{10.7} = 70 \qquad K = 10^7$$

CONTOURS OF HELIUM DENSITY AT ALTITUDE 320
JUNE SOLSTICE
$F_{10.7} = 70$ $K = 10^7$

Fig. 9f

CONTOURS OF HELIUM DENSITY AT ALTITUDE 380
JUNE SOLSTICE

$F_{10.7} = 70 \qquad K = 10^7$

Fig. 9

CONTOURS OF HELIUM DENSITY AT ALTITUDE 430
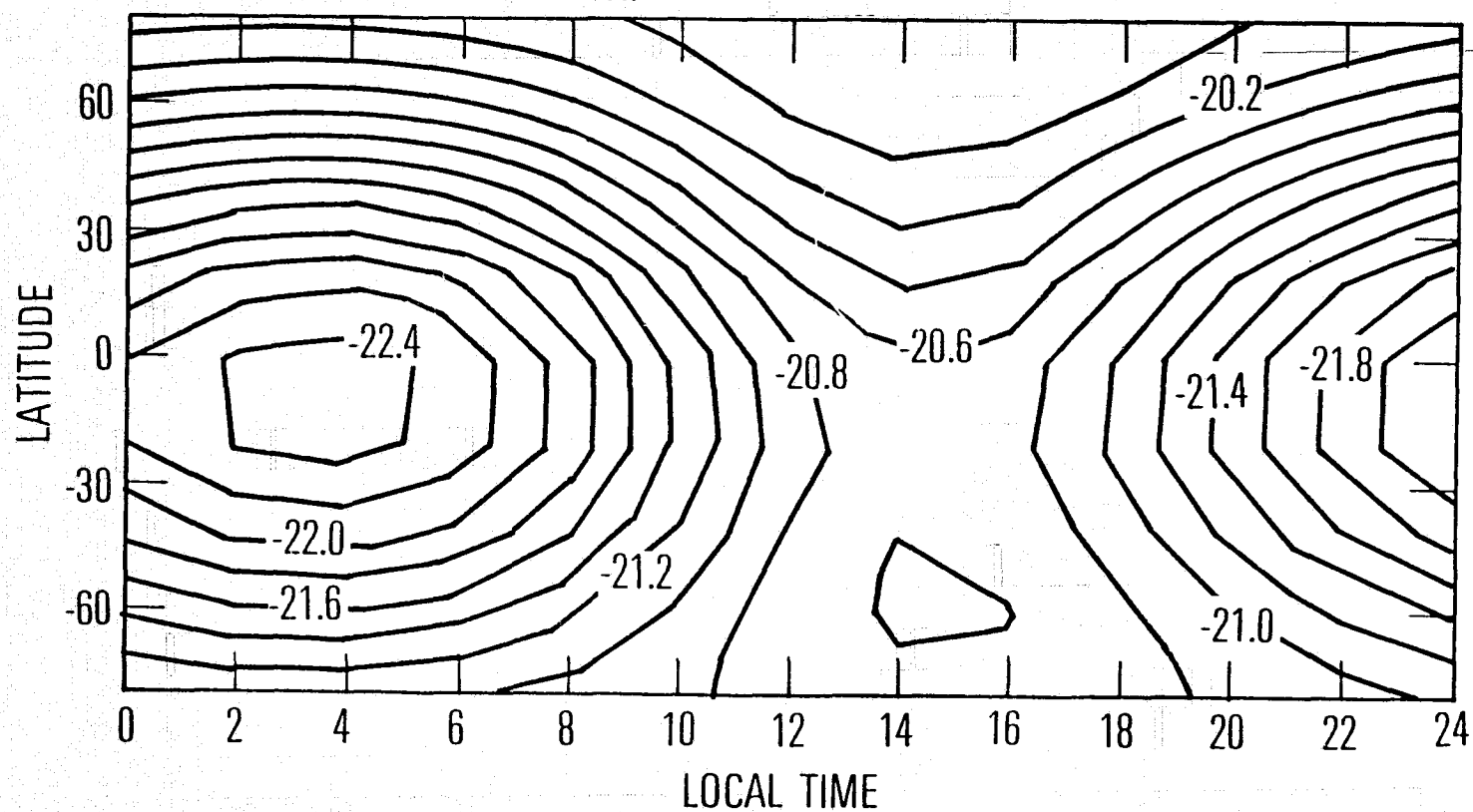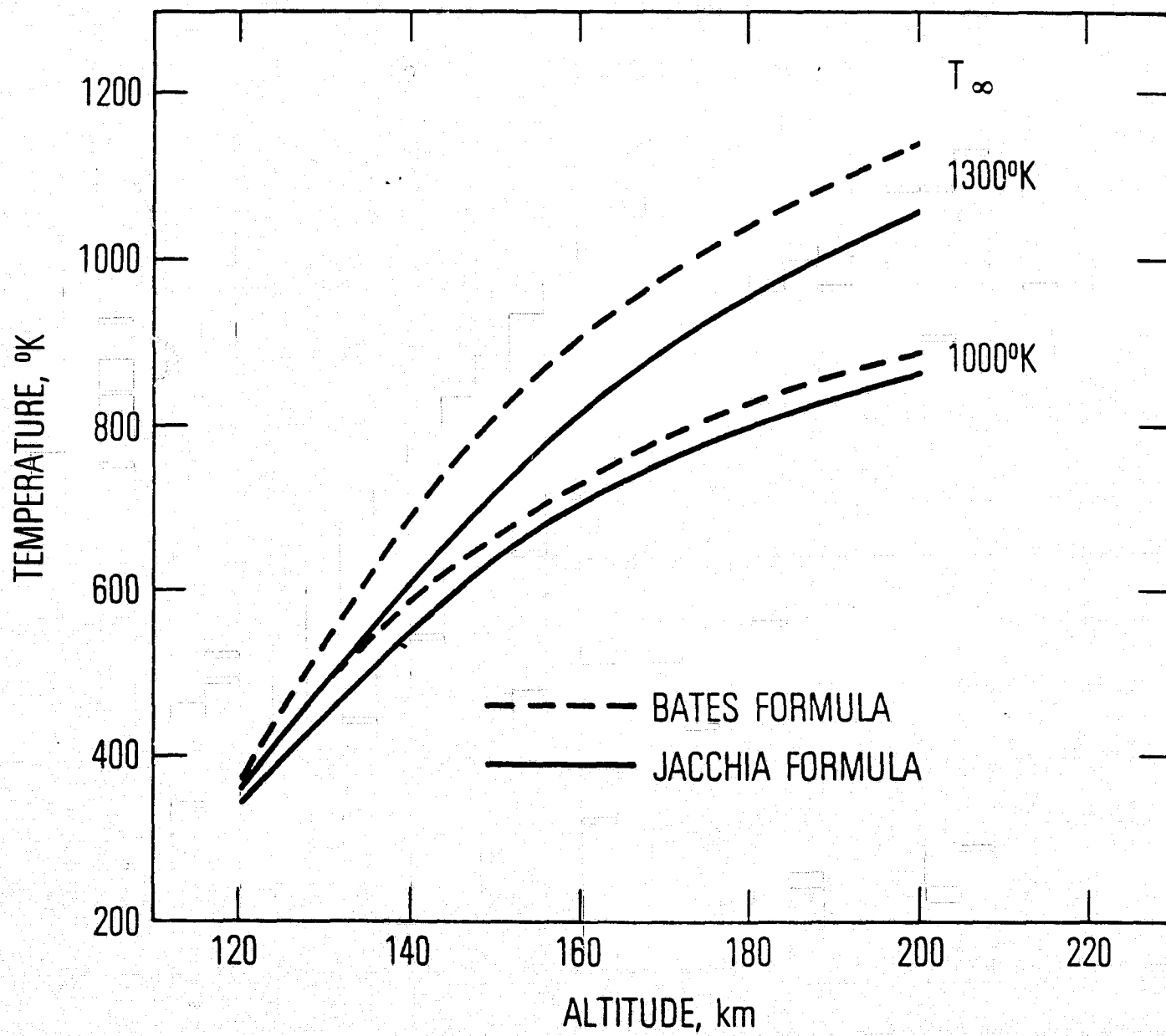JUNE SOLSTICE
$F_{10.7} = 70$ $K = 10^7$

CONTOURS OF HELIUM DENSITY AT ALTITUDE 470
JUNE SOLSTICE

$$F_{10.7} = 70 \qquad K = 10^7$$

CONTOURS OF HELIUM DENSITY AT ALTITUDE 490
JUNE SOLSTICE
$F_{10.7} = 70 \qquad K = 10^7$

Fig. 10

Fig. 11

CONTOURS OF ARGON DENSITY AT ALTITUDE 95
JUNE SOLSTICE
$F_{10.7} = 100$ $K = 10^7$

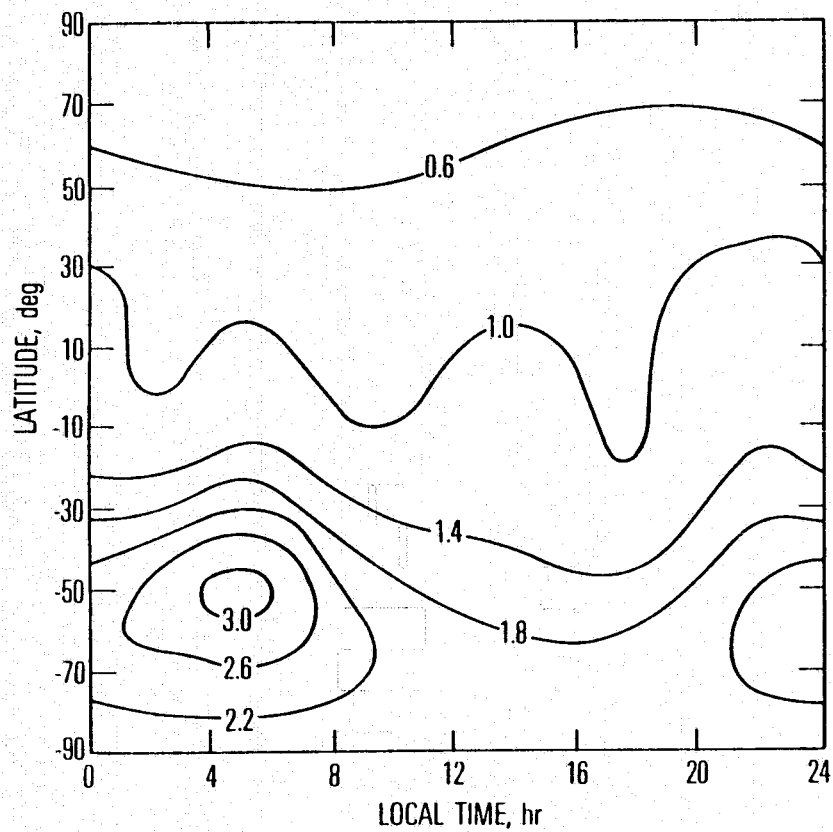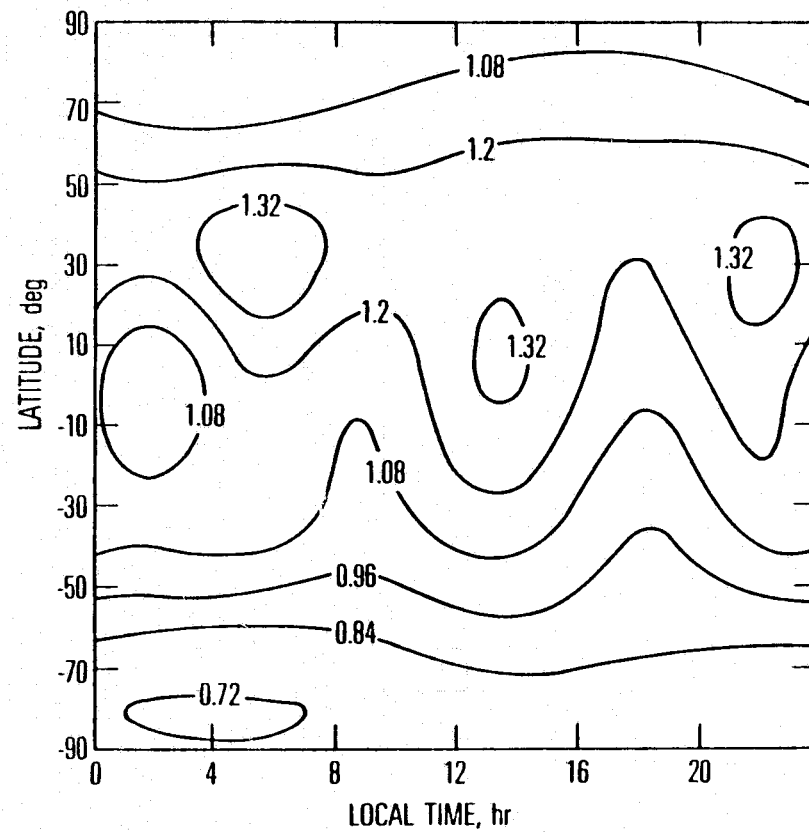CONTOURS OF ARGON DENSITY AT ALTITUDE 155
JUNE SOLSTICE

$F_{10.7} = 100 \qquad K = 10^7$

Fig. 125

CONTOURS OF ARGON DENSITY AT ALTITUDE 206
JUNE SOLSTICE

$F_{10.7} = 100 \qquad K = 10^7$

CONTOURS OF ARGON DENSITY AT ALTITUDE 263
JUNE SOLSTICE
$F_{10.7} = 100 \qquad K = 10^7$

CONTOURS OF ARGON DENSITY AT ALTITUDE 320
JUNE SOLSTICE

$F_{10.7} = 100 \qquad K = 10^7$

CONTOURS OF ARGON DENSITY AT ALTITUDE 430
JUNE SOLSTICE

$$F_{10.7} = 100 \qquad K = 10^7$$

Fig. 13

(a)

(b)

Fig. 4

(a)

(b)

Fig. 15

Fig. 16